SQ-A: A Collision-triggered Starburst in the Intragroup Medium of Stephan's Quintet

C K Xu, C. Cheng, M S Yun, P N Appleton, B H C Emonts, J. Braine, S C Gallagher, P. Guillard, U. Lisenfeld, E. O'sullivan, et al.

The Astrophysical Journal, 991:197 (17pp), 2025 October 1 https://doi.org/10.3847/1538-4357/adfbf6

SQ-A: A Collision-triggered Starburst in the Intragroup Medium of Stephan's Quintet

C. K. Xu[1,2], C. Cheng[1,2,3], M. S. Yun[4], P. N. Appleton[5], B. H. C. Emonts[6], J. Braine[7], S. C. Gallagher[8], P. Guillard[9,10], U. Lisenfeld[11,12], E. O'Sullivan[13], F. Renaud[14,15], P. Aromal[8,16], P.-A. Duc[17], A. Labiano[18], and A. Togi[19]

[1] Chinese Academy of Sciences South America Center for Astronomy, National Astronomical Observatories, CAS, Beijing 100101, People's Republic of China
[2] National Astronomical Observatories, Chinese Academy of Sciences, 20A Datun Road, Chaoyang District, Beijing 100101, People's Republic of China
[3] CAS Key Laboratory of Optical Astronomy, National Astronomical Observatories, Chinese Academy of Sciences, Beijing 100101, People's Republic of China
[4] Department of Astronomy, University of Massachusetts, Amherst, MA 01003, USA
[5] Caltech/IPAC, MC 314-6, 1200 E. California Blvd., Pasadena, CA 91125, USA
[6] National Radio Astronomy Observatory, 520 Edgemont Road, Charlottesville, VA 22903, USA
[7] Observatoire de Bordeaux, UMR 5804, CNRS/INSU, BP 89, 33270 Floirac, France
[8] Institute for Earth and Space Exploration, Western University, 1151 Richmond St., London, ON N6A 3K7, Canada
[9] Sorbonne Université, CNRS, UMR 7095, Institut d'Astrophysique de Paris, 98bis bd Arago, 75014 Paris, France
[10] Institut Universitaire de France, Ministère de l'Enseignement Supérieur et de la Recherche, 1 rue Descartes, 75231 Paris Cedex 05, France
[11] Departamento de Física Teórica y del Cosmos, Universidad de Granada, 18071 Granada, Spain
[12] Instituto Carlos I de Física Teórica y Computacional, Facultad de Ciencias, 18071 Granada, Spain
[13] Center for Astrophysics | Harvard & Smithsonian, 60 Garden Street, Cambridge, MA 02138, USA
[14] Observatoire Astronomique de Strasbourg, Université de Strasbourg, CNRS UMR 7550, F-67000 Strasbourg, France
[15] University of Strasbourg Institute for Advanced Study, 5 allée du Général Rouvillois, F-67083 Strasbourg, France
[16] Physics and Astronomy Department, University of Western Ontario, 1151 Richmond Street, London, N6A 3K7, Ontario, Canada
[17] Université de Strasbourg, CNRS, Observatoire astronomique de Strasbourg (ObAS), UMR 7550, 67000 Strasbourg, France
[18] Telespazio UK S.L. for the European Space Agency (ESA), ESAC, Spain
[19] Texas State University, 601 University Dr., San Marcos, TX 78666, USA

Received 2025 May 20; revised 2025 August 13; accepted 2025 August 13; published 2025 September 29

Abstract

We present new observational evidence supporting the hypothesis that SQ-A, a starburst in the intragroup medium (IGrM) of Stephan's Quintet (SQ), is triggered by a high-speed collision between two gas systems, one associated with the IGrM ($v \sim 6900\,\mathrm{km\,s^{-1}}$) and another with the intruder galaxy NGC 7318b ($v \sim 6000\,\mathrm{km\,s^{-1}}$). The new CO(2–1) data set from the Atacama Large Millimeter/submillimeter Array has angular resolutions between 0.″2 and 7.″0 and the new Very Large Array H I data cube has an angular resolution of 6.″6 × 7.″9. The CO maps show that the two gas systems are bridged by another system with an intermediate velocity of ∼6600 km s^{-1}, whereas the H I data show that the component of $v \sim 6600\,\mathrm{km\,s^{-1}}$ fits well into a gap in the more extended $v \sim 6000\,\mathrm{km\,s^{-1}}$ component, albeit with a displacement of ∼5 kpc. Both the bridge and the complementary distributions between different gas systems are common features of starbursts triggered by cloud–cloud collision. An analysis of clumps (sizes of 100–200 pc) reveals very diversified star formation (SF) activity in clumps belonging to different kinematic systems, with the molecular gas depletion time of the $v \sim 6900\,\mathrm{km\,s^{-1}}$ clumps being more than 10 times longer than that of the $v \sim 6600\,\mathrm{km\,s^{-1}}$ clumps. The results are consistent with a scenario in which the enhanced SF activity (and the starburst) in the system of $v \sim 6600\,\mathrm{km\,s^{-1}}$ is due to gas compression generated in cloud–cloud collisions, whereas the suppression of SF in the $v \sim 6900\,\mathrm{km\,s^{-1}}$ system is due to vortices (i.e. gas rotation) generated in more complex collisions involving dense clouds and diffuse intercloud gas associated with high-speed shocks.

Unified Astronomy Thesaurus concepts: Hickson compact group (729); Circumgalactic medium (1879); Intergalactic medium (813); Interacting galaxies (802); Millimeter astronomy (1061); Galaxy groups (597); Galaxy collisions (585); Shocks (2086); H I line emission (690); Star formation (1569)

1. Introduction

Starbursts are rarely found in compact groups of galaxies, which are aggregates of four to eight galaxies with implied space densities as high as those in cluster cores (P. Hickson 1982; K. E. Johnson et al. 2007). This is remarkably different from galaxy mergers, where interaction-induced starbursts are very common (D. B. Sanders & I. F. Mirabel 1996; R. C. Kennicutt 1998). Indeed many interacting galaxies in compact groups have their star formation (hereafter SF) activity quenched rather than enhanced (K. Alatalo et al. 2014). SQ-A, a starburst in the intragroup medium (IGrM) of the famous compact group Stephan's Quintet (hereafter SQ), is quite unique. As a prototype of compact groups, SQ is undergoing a very complex web of interactions between member galaxies and various constituents of the IGrM (M. Moles et al. 1997; J. W. Sulentic et al. 2001), which in turn have triggered some spectacular activities such as a ∼40 kpc large-scale shock (shown as a large radio and X-ray ridge; R. J. Allen & J. W. Hartsuiker 1972; G. Trinchieri et al. 2003; C. K. Xu et al. 2003; E. O'Sullivan et al. 2009) and the IGrM starburst SQ-A.

SQ-A was discovered as a bright infrared source by C. Xu et al. (1999) using the Infrared Space Observatory (ISO; M. F. Kessler et al. 1996). Because of the relatively low

resolution (∼10″) of the ISO observation, SQ-A originally included the entire region beyond the northern tip of the large-scale shock (R. J. Allen & J. W. Hartsuiker 1972; G. Trinchieri et al. 2003; C. K. Xu et al. 2003; E. O'Sullivan et al. 2009). The SQ-A region, also known as the "northern starburst region" in the literature (S. C. Gallagher et al. 2001; K. Fedotov et al. 2011), is faint in optical and near-infrared (NIR) continuum (C. Xu et al. 1999) though relatively bright in Hα (H. Arp 1995; M. Moles et al. 1998; J. Iglesias-Paramo & J. M. Vilchez 2001; C. Mendes de Oliveira et al. 2001; S. Duarte Puertas et al. 2019). In contrast, it is very bright in the ISO 15 μm band, with a peak surface brightness second only to that of the Sy2 nucleus of NGC 7319, which is the most massive galaxy of SQ. The more recent observations, particularly the optical spectroscopic imaging observations by S. Duarte Puertas et al. (2019), reveal that the SQ-A region is dominated by a compact starburst of size ∼5″ (∼2 kpc) and a velocity of ∼6680 km s^{-1} (hereafter SQ-A starburst); at the same time it contains many other star formation regions of different velocities. According to C. K. Xu et al. (2005), the total star formation rate (SFR) of SQ-A is 1.34 $M_{\odot}$ yr^{-1}, comparable to that of the large Sb galaxy NGC 7319 (1.98 $M_{\odot}$ yr^{-1}). The very low NIR luminosity of SQ-A indicates a young age (∼10^7 yr) for the starburst (C. Xu et al. 1999), consistent with the ages of the star clusters found in the region (S. C. Gallagher et al. 2001; K. Fedotov et al. 2011). Although the general morphology of the SQ-A region has been reproduced by numerical simulations (F. Renaud et al. 2010; J.-S. Hwang et al. 2012), its starburst nature has not.

There has been a debate on how the SQ-A starburst is triggered. C. Xu et al. (1999) argued that the starburst is triggered by a collision of two gas systems, one with a velocity of ∼6600 km s^{-1} associated with the IGrM and the other with a velocity of ∼6000 km s^{-1} associated with the intruder galaxy NGC 7318b, because both the H I data (G. S. Shostak et al. 1984) and Hα data (C. Xu et al. 1999; C. Mendes de Oliveira et al. 2001) show overlaps of the two systems at the position of SQ-A. However, from the beginning, this interpretation has been challenged by a difficult question: if high-speed collision between gas systems can trigger a starburst, why is no starburst found in the shock region associated with the large radio and X-ray ridge? It is well established that the large-scale shock is triggered by an ongoing collision between the IGrM and the intruder NGC 7318b (R. J. Allen & J. W. Hartsuiker 1972; M. Moles et al. 1997; J. W. Sulentic et al. 2001; C. K. Xu et al. 2003; P. N. Appleton et al. 2006, 2013, 2023; P. Guillard et al. 2009, 2022; M. E. Cluver et al. 2010). According to M. E. Cluver et al. (2010), the shocks and turbulence produced by the high-speed collision are more likely to suppress the SF rather than trigger a starburst. An alternative model to explain the starburst in SQ-A was proposed by C. Mendes de Oliveira et al. (2001), who listed the two kinematic systems in SQ-A as two separate tidal dwarf candidates, suggesting that the SF in SQ-A is tidally induced and the collocation of multiple kinematic components in the region is due to a projection effect.

Can shocks and turbulence powered by high-speed collisions trigger starbursts and at the same time suppress the SF activity elsewhere in the involved gas systems? What are the physical mechanisms behind these processes? The answer to these questions may have far-reaching implications for our understanding of the SF in gas systems, particularly the triggered SF (B. G. Elmegreen 1998), which may play an important role in the SF activity in interacting galaxy systems. In this paper, using the new high-resolution CO data obtained by the Atacama Large Millimeter/submillimeter Array (ALMA) and H I data from the B, C, and D arrays of the Karl G. Jansky Very Large Array (VLA), we aim to answer these questions. In particular, we revisit the question: is SQ-A triggered by a collision of the IGrM and the intruder? Significant progress has been achieved recently in cloud–cloud collision (hereafter CCC) theories (A. Habe & K. Ohta 1992; K. Takahira et al. 2014; D. Abe et al. 2021; R. Maeda et al. 2021, 2024), which can provide powerful tools for our investigation. Encouraged by successful applications of the CCC models to large extragalactic SF regions such as the overlap region of Antennae Galaxies and 30 Doradus in the Large Magellanic Cloud (Y. Fukui et al. 2017; K. Tsuge et al. 2021a, 2021b; K. Tsuge et al. 2024), we are motivated to find more signatures of collision-triggered SF in SQ-A.

The paper is organized as follows: after this introduction, we present the observational data sets used in this work in Section 2. Our results revealing new evidence for collisions between different gas systems in SQ-A are presented in Section 3. In Section 4 (and the Appendix) we carry out an analysis on the properties of clumps (size ∼100–200 pc), aiming to probe the cloud-level physical conditions leading to active SF or suppression of it in SQ-A. Section 5 is devoted to discussions. In Section 6 we present our conclusions. Throughout the paper we assume a distance of 94 Mpc (1″ corresponds to 0.45 kpc). The velocities are in the optical redshift convention and in the reference frame of the local standard of rest.

2. Observations

2.1. ALMA Observations of CO(2–1)

CO(2–1) data of different angular resolutions and different coverages are utilized in this paper. They are obtained using ALMA in different configurations. Mosaic observations using the Atacama Compact Array (ACA) cover a region of ∼10 arcmin^2 that includes all five member galaxies of SQ and most of the IGrM, with a synthetic beam of 8.″0 × 7.″0 (see B. H. C. Emonts et al. 2025). We added to this new observations of similar mosaic coverage but higher (∼0.″6) resolution made with the ALMA 12 m array in C43-3 configuration from 2024 August 16–September 5 (ID: 2023.1.00177.S; PI: Appleton) with a total on-source integration time of 6.4 hr (hereafter TM2 data). These data were calibrated by the ALMA calibration pipeline version 2023.1.0.124 for Cycle-10 (T. R. Hunter et al. 2023) and delivered as calibrated MeasurementSets by the North American ALMA Science Center. We used the Common Astronomy Software Applications (CASA) version 6.6.4.34 (CASA Team et al. 2022) to image the combined pointings of the ALMA and ACA mosaics that include the SQ-A region (TM2+ACA data). The imaging was done by using a Briggs weighting with robustness 0.5 (D. S. Briggs 1995) and applying a multiscale clean with scales 0, 5, 10, 25, and 60 pixels of 0.″1 down to a threshold of 3.5 mJy beam^{-1}. This resulted in a line-data cube with an angular resolution of 1.″0 × 0.″66 at position angle (PA) –12.°7, channel width of 15 km s^{-1}, and an rms noise of 0.85 mJy beam^{-1} in the center

of the SQ-A field. A primary beam correction was applied, which increased the rms noise toward the edges of the field.

Finally, the ALMA data of even higher resolution in a single-pointing field centered on the SQ-A starburst, namely "Field 4" of P. N. Appleton et al. (2023), were taken from the ALMA archive (ID: 2015.1.00241.S; PI: P. Guillard) and reprocessed with CASA using the default script SCRIPTFORPI.PY to obtain the calibrated MeasurementSets. Then we clean the image by TCLEAN with the parameters WEIGHTING = "NATURAL." The final data cube reaches an rms of about 0.66 mJy beam^{-1} and channel width of 4 km s^{-1}, with a beam size of $0\farcs38 \times 0\farcs23$ and PA $= -0\fdg86$. Compared to the original Field 4 data cube presented by P. N. Appleton et al. (2023), the reprocessed cube has the following improvements: (1) a velocity bin width of 4 km s^{-1} instead of 20 km s^{-1}; (2) a much larger field of view of size $= 38''$ (though results outside the $22''$ primary beam must be taken with caution). In this work, we assume a CO conversion factor $\alpha_{\rm CO10} = 1.0\,M_\odot$ (K km s^{-1} pc^2)$^{-1}$ and a CO(2–1) to CO(1–0) luminosity ratio $r_{21} = L'_{\rm CO}(2-1)/L'_{\rm CO}(1-0) = 0.34$ (B. H. C. Emonts et al. 2025). It is worth noting that both $\alpha_{\rm CO10}$ and r_{21} are quite uncertain. A detailed discussion of these uncertainties is given in Section 5.3.

2.2. VLA Observations of the H I 21 cm Line

The VLA B-array observations of the 21 cm H I transition were carried out for a total of 40 hr between 2005 May 27 and June 5 as part of the AY155 program. The spectrometer setup used was identical to the earlier C- and D-array observations reported by L. Verdes-Montenegro et al. (2001) and B. A. Williams et al. (2002), with a velocity resolution of 21.5 km s^{-1}. The nearby VLA calibrator 2234+282 was observed frequently to track the instrument gain, and 3C 48 (0134+329) was observed for the bandpass and flux calibration. All of the data were calibrated using the standard VLA calibration procedure in AIPS and imaged using IMAGR. In order to achieve better UV coverage and better sensitivity, we combine these data with those obtained with the VLA C and D arrays (beam $=19\farcs4 \times 18\farcs6$; B. A. Williams et al. 2002). The final H I data cube has a synthesized beam of $7\farcs9 \times 6\farcs7$ (FWHM) and a velocity coverage of 5550–6885 km s^{-1}.

2.3. JWST MIRI Images

Archived images in three MIRI bands of the James Webb Space Telescope (JWST) are downloaded from the Dawn JWST Archive (DJA) website[20,21] (F. Valentino et al. 2023). These are the F770W, F1000W, and F1500W bands centered at 7.7 μm, 10 μm, and 15 μm with angular resolutions of $0\farcs27$, $0\farcs33$, and $0\farcs49$, respectively (D. Dicken et al. 2024). The astrometric precision of the MIRI images matches well with that of GAIA DR3, which is of the order of 1 mas (M. Libralato et al. 2024). The F770W and F1000W data are used only in the inset of Figure 1 for illustration. The 15 μm image taken from the F1500W data is used in the analysis of clumps (Section 4). The 15 μm emission is dominated by thermal emission of warm dust heated by massive stars, and therefore is a good SF indicator (C. Xu et al. 1999). In principle, the 7.7 μm image (dominated by emission from polycyclic aromatic hydrocarbons) and 10 μm image (warm dust emission) may also be used to study SF. They have better angular resolutions than the 15 μm image and are also insensitive to dust extinction, which can be substantial in SQ-A (S. Duarte Puertas et al. 2021). However, both F770W and F1000W are significantly contaminated by shock-excited warm H_2 line emissions and therefore are disfavored: the F770W filter includes the H2S(4) line at 8.025 μm and the F1000W filter the H2S(3) line at 9.665 μm. Both H_2 lines are bright in SQ (M. E. Cluver et al. 2010; P. N. Appleton et al. 2023). It is worth noting that the F1500W filter also includes the bright emission line [N III] 15.56 μm, which is dominantly associated with SF regions. It may not affect the 15 μm flux as an SFR indicator significantly if the [N III] 15.56 μm-to-continuum ratio is relatively constant.

[20] https://s3.amazonaws.com/grizli-v2/JwstMosaics/v4/index.html
[21] https://zenodo.org/records/8370018

3. Collision of Systems Associated with IGrM and Intruder

In Figure 1 contours of the VLA H I maps of resolution $= 7\farcs9 \times 6\farcs7$ (white contours) and of resolution $=19\farcs4 \times 18\farcs6$ (magenta contours), and contours of the ACA CO(2–1) map (yellow contours, resolution $= 8\farcs0 \times 7\farcs0$) are overlaid on a three-color image of the UV and optical emissions (blue: NUV, C. K. Xu et al. 2005; green: deep g-band, P.-A. Duc et al. 2018; red: H_α, C. Xu et al. 1999). A more comprehensive comparison of the CO and H I data in the entire SQ will be presented in a future paper (C. Cheng et al. 2025, in preparation). In this paper we will concentrate on the SQ-A region, shown by the small yellow box (size $= 36'' \times 30''$) in the upper right quadrant of the figure. The inset in the upper right corner is a three-color JWST image (blue: 7.7 μm; green: 10 μm; red: 15 μm; K. M. Pontoppidan et al. 2022) of the SQ-A field, which reveals the detailed morphology of the SF regions behind the CO and H I contours in the main figure.

In Figure 2, the CO(2–1) and H I spectra extracted from the CO(2–1) cube of ALMA ACA and the H I cube of VLA B, C, and D arrays in the SQ-A region (the yellow box in Figure 1) are presented. It is worth noting that the two cubes have very similar angular resolutions (ACA CO(2–1): $8\farcs0 \times 7\farcs0$; VLA B, C, and D arrays H I: $7\farcs9 \times 6\farcs7$) and therefore the comparison between them is robust. The CO spectrum shows clearly three components. Following the literature (G. S. Shostak et al. 1984; B. A. Williams et al. 2002; C. Cheng et al. 2023), we call them the 6000, 6600, and 6900 components, which are in velocity ranges of 5900–6100, 6500–6800, and 6800–7000 km s^{-1}, respectively. As shown in Table 1, the 6900 component has the highest molecular gas mass $M_{\rm mol}$, which is 1.9 and 1.5 times $M_{\rm mol}$ of the 6000 and 6600 components, respectively. For the 6000 and 6600 components the H I is much more abundant than the molecular gas: $M_{\rm HI}$ is about 10 times higher than $M_{\rm mol}$ for both components. Unfortunately the 6900 component is not covered by the VLA H I observations. Preliminary results of a new MeerKAT observation of H I emission in SQ (unpublished) indicate that the H I gas in the SQ-A region does have a 6900 component, albeit with $M_{\rm HI}$ less than half of that of the 6000 component (K. Rajpurohit 2025, private communication). Together with the data in Table 1, this suggests that the gas associated with the 6900 component is denser than that associated with the 6000 component because the former has an $M_{\rm mol}$-to-$M_{\rm HI}$ ratio $\sim$4 times higher than the latter. The H I 6900 component seems to be more extended than its CO counterpart but, given the larger beam of the MeerKAT map ($\sim 15''$) compared to that

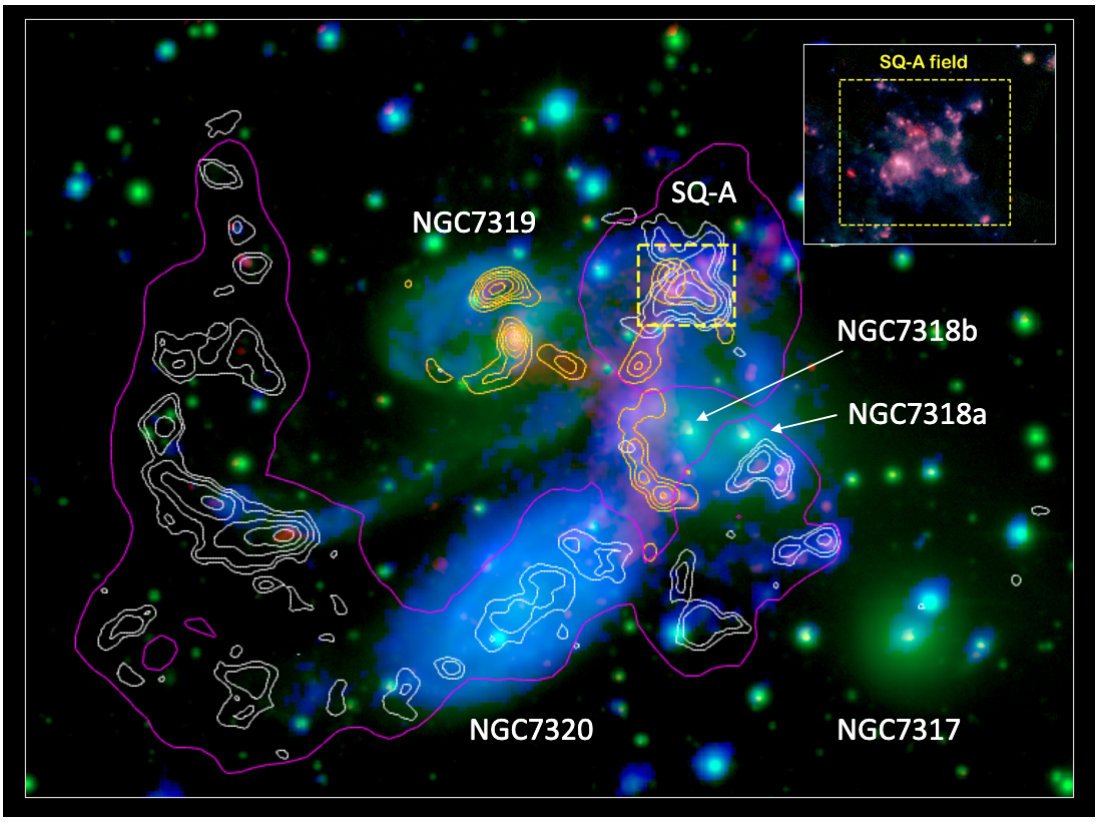

Figure 1. Contour maps of the H I 21 cm emission obtained using the VLA B, C, and D arrays (white contours, resolution: $7\farcs9 \times 6\farcs7$) and the VLA C and D arrays (magenta contours, resolution: $19\farcs4 \times 18\farcs6$), and that of the CO(2–1) emission obtained using the ALMA ACA array (yellow contours, resolution: $8\farcs0 \times 7\farcs0$) overlaid on a three-color image of the UV and optical emissions (blue: NUV, C. K. Xu et al. 2005; green: deep g-band, P.-A. Duc et al. 2018; red: Hα, C. Xu et al. 1999). Note that the ACA CO(2–1) contours in the shock region look orange because of the colored background. The small box delineated by yellow dashed lines (size $= 36'' \times 30''$) marks the location of the "SQ-A region" studied in this paper. The inset in the upper right corner is a three-color JWST image (blue: 7.7 μm; green: 10 μm; red: 15 μm) of the SQ-A region.

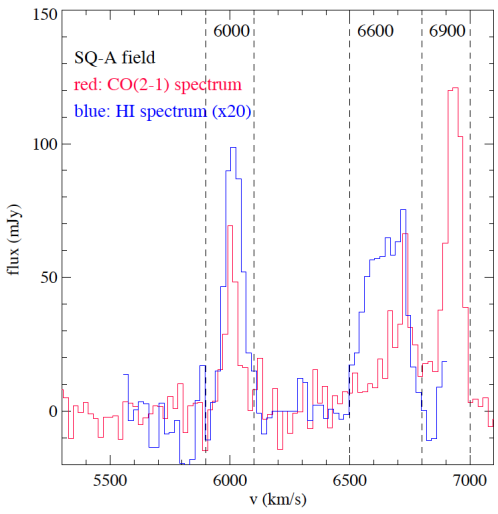

Figure 2. Spectra of the CO(2–1) and the H I (scaled up by a factor of 20) in the SQ-A region.

of the ACA, caution is needed about any direct comparison at this stage.

The left panel of Figure 3 shows the spatial distributions of the three kinematic components of CO using contours of their ACA maps, overlaid on a JWST 15 μm image. The 6900 and 6000 components do not overlap with each other but are bridged by the the 6600 component. Many SF regions, including the SQ-A starburst that corresponds to the brightest 15 μm peak near the center of the figure, are associated with the CO gas. However, several SF regions in the upper right corner of the figure (near the edge of the ACA coverage as shown by the purple dashed line), which are associated with the 6000 component (S. Duarte Puertas et al. 2019), are not significantly detected by the ACA observations because their CO emission is only on the 2σ level ($\sigma = 0.39$ Jy beam^{-1} km s^{-1}).

The right panel of Figure 3 presents the H I gas distributions of only the 6000 and 6600 components, while the 6900 component is missed by the H I observations. The H I distributions of both components are more extended than their CO counterparts. Very interestingly, the 6600 H I seems to be located in a gap of the much more extended 6000 H I gas. Figure 4 demonstrates that, when the 6600 H I map is shifted eastward relative to the 6000 H I map by $12''$ (corresponding to a linear scale of $\sim$5 kpc for a distance of 94 Mpc), the maps of the two components become very "complementary" in the sense that the 6600 map fits nearly perfectly to the gap in the 6000 map. Note that the $\sim$5 kpc transverse displacement, without which the complementary nature of the distributions of the two components is not easily recognizable, is the projection of a three-dimensional relative movement between the two components. This is consistent with the CCC scenario (see, e.g., Figure 8 of K. Tsuge et al. 2021b). This new piece of supporting evidence enables us to conclude with high confidence that the multiple kinematic components in SQ-A

Table 1
Properties of Three Kinematic Components of Gas in the SQ-A Region

	6000	6600	6900
v range (km s^{-1})	5900–6100	6500–6800	6800–7000
f_{CO}(2–1) (Jy km s^{-1})[a]	4.8 ± 0.5	6.0 ± 0.6	8.8 ± 0.9
M_{mol} ($10^8 \times M_\odot$)[b]	0.75 ± 0.38	0.93 ± 0.47	1.4 ± 0.7
v_{CO} (km s^{-1})	6010 ± 32	6719 ± 41	6930 ± 33
$W20_{CO}$ (km s^{-1})[c]	76	132	112
f_{HI} (Jy km s^{-1})[d]	0.46 ± 0.07	0.65 ± 0.10	⋯
M_{HI} ($10^9 \times M_\odot$)	0.95 ± 0.14	1.35 ± 0.20	⋯
v_{HI} (km s^{-1})	6020 ± 31	6645 ± 63	⋯
$W20_{HI}$ (km s^{-1})[e]	129	280	⋯
SFR ($M_\odot$ yr^{-1})[f]	0.37	0.98	0.07
t_{dep} (10^8 yr)[g]	2.02	0.95	19.5

Notes.
[a] Integrated CO(2–1) flux. A 10% calibration uncertainty is assumed, which dominates the errors.
[b] Molecular gas mass estimated from the CO(2–1) data assuming the CO conversion factor $\alpha_{CO10} = 1.0\ M_\odot\ (\mathrm{K\ km\ s^{-1}\ pc^2})^{-1}$ and the CO(2–1) to CO(1–0) luminosity ratio $r_{21} = L'_{CO(2-1)}/L'_{CO(1-0)} = 0.34$ (B. H. C. Emonts et al. 2025). A 50% uncertainty is assumed for α_{CO10}, which dominates the errors.
[c] CO(2–1) line width measured at 20% of peak.
[d] Integrated H I flux. A 15% calibration uncertainty is assumed, which dominates the errors.
[e] H I line width measured at 20% of peak.
[f] The star formation rate estimated using the extinction-corrected Hα luminosities of the H II regions (including only SF-dominated regions and excluding the composite regions) in the SQ-A region (S. Duarte Puertas et al. 2021).
[g] Depletion timescale of molecular gas: $t_{dep} = M_{mol}/\mathrm{SFR}$.

are colliding with each other and their collocation in the region is not merely a projection effect.

Y. Fukui et al. (2021) have shown that there are two key common properties in all cases of CCC-triggered SF: (1) gas systems involved in the collision show complementary distributions, with relative displacement explainable by relative motion and projection effects (as in the case shown in Figure 4), and (2) a "bridge" (an system at intermediate velocity) lies in between the colliding systems. It appears that kinematic components in SQ-A have both of these properties (Figures 3 and 4). This suggests the following scenario: the SQ-A starburst is triggered by a collision between the 6900 component (associated with the IGrM) and the 6000 component (associated with the intruder galaxy NGC 7318b). It appears that only a part of the 6900 component as well as a part of the 6000 component are involved in the collision. During the collision the 6900 gas, which is likely to be denser and more compact than the 6000 gas, is decelerated and compressed, and this decelerated and compressed gas becomes the 6600 component in which the SQ-A starburst ($v \sim 6680$ km s^{-1}) is triggered. At the same time, the 6000 gas involved in the collision is swept into the 6600 component and/or dispersed, leaving a gap in the 6000 map at the place where the 6600 component crashes through. The displacement shown in Figure 4, which is ~5 kpc in linear scale, suggests an age of the collision of a few 10^7 yr (assuming a transverse relative velocity of a few hundred km s^{-1} between the colliding systems), consistent with the estimated timescale for the age of the encounter between the intruder and SQ (J. W. Sulentic et al. 2001). We will discuss this scenario in more depth in Section 5.1.

In Table 1, we present the properties of the three kinematic components. It appears that, among them, the 6600 component has the broadest CO and H I line widths, consistent with the hypothesis that it is formed in the postshock gas after the collision between the other two components. The SFR data are adopted from S. Duarte Puertas et al. (2021) after adjusting the difference between the adopted distances of SQ (they assume a distance of 88.6 Mpc). The total SFR of SQ and the SFR of SQ-A estimated from extinction-corrected Hα luminosities of the H II regions are both consistent with the UV-and-IR estimated values of C. K. Xu et al. (2005). In addition, S. Duarte Puertas et al. (2021) provided the velocity information for the SF regions and distinguished composite regions (shock-excited) from SF regions using the Baldwin–Phillips–Telervich diagrams. The 6600 component has the highest SFR, dominated by the starburst. The 6000 component also has a sizable SFR though it is about a factor of 3 lower than that of the 6600 component. The 6900 component has very little SF; its SFR is more than an order of magnitude lower than that of the 6600 component.

4. Properties of Clumps of Molecular Gas in SQ-A

4.1. Clumps Extracted from the High-resolution CO(2–1) Data Cube

In order to probe at the cloud level the physical conditions that lead to the conspicuous difference in SF activity in different kinematic components (Table 1), in this section we study "clumps" extracted from the high-resolution CO(2–1) data cube in Field 4 (P. N. Appleton et al. 2023), exploiting the algorithm "Fellwalker" developed by D. Berry (2015). According to C. Li et al. (2020), Fellwalker shows high completeness and accuracy compared to other clump identification algorithms. Fellwalker works as follows: First, it selects in a 3D cube all pixels that are above a certain threshold, which we set at 1σ above the background level. Second, it links each of these pixels to a local maximum along the steepest gradient. Finally, it identifies each individual clump as the collection of all pixels that end up at the same maximum. Details of the clump identification procedure and definitions of various parameters of the clumps are presented in the Appendix.

In total 36 clumps are identified in Field 4. They are listed in Table A1 in the Appendix and plotted in Figure 5. The figure also shows contour maps of CO(2–1) overlaid on a JWST 15 μm image. Solid contours are for the combined TM2+ACA data (beam = $1\farcs0 \times 0\farcs66$) and dashed contours mark the boundaries of ACA detections (beam = $8\farcs0 \times 7\farcs0$). There are good correspondences between locations of the clumps and peaks of the intermediate-resolution CO map (TM2+ACA) for the 6600 and 6900 components. No clumps are found for the 6000 component in the northwestern part because this region is outside the primary beam of Field 4 (whose boundary is marked by the black dashed–dotted line) and the sensitivity becomes too low. Around the SQ-A starburst ($v = 6680$ km s^{-1}), there is a cluster of 6600 clumps squeezed inside a compact configuration in the TM2+ACA map. Interestingly, this 6600 configuration is surrounded by a couple of low-level contours of the 6900 and 6000 components as well as two 6900 clumps, consistent with the hypothesis that there is an ongoing interaction among these components at this location. A couple of 15 μm emission regions near the center of the figure are

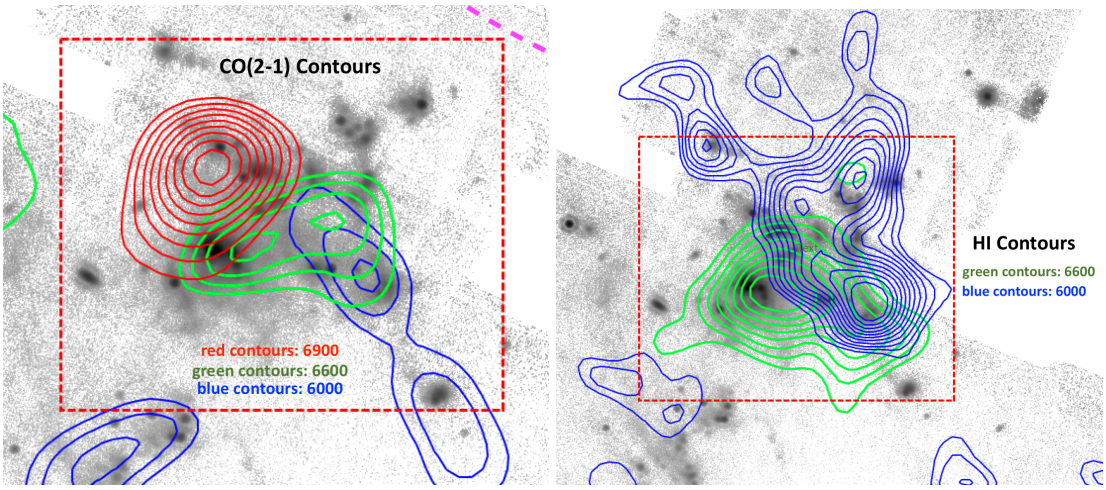

Figure 3. Left: contours of the ALMA ACA map of CO(2–1) in the SQ-A region, overlaid on a JWST 15 μm image. The blue, green, and red contours are for the 6000, 6600, and 6900 components, respectively (contour levels: 1.3, 1.4, 1.5, … Jy beam^{-1} km s^{-1}). The three maps have rms of 0.36, 0.41, and 0.39 Jy beam^{-1} km s^{-1}, respectively. The purple dashed line near the upper right corner of the figure shows the boundary of the ACA observation. The inner box delineated by the red dashed lines marks the location of the SQ-A region. Right: contours of the map of H I from the VLA B, C, and D arrays overlaid on the JWST 15 μm image. Blue and green contours are for the 6000 and 6600 components, respectively (contour levels at 0.04, 0.05, 0.06, … Jy beam^{-1} km s^{-1}). Both maps have the same rms = 0.01 Jy beam^{-1} km s^{-1}. Again the red box delineates the SQ-A region.

not associated with clumps or peaks in the intermediate-resolution CO map. They correspond to the composite regions #126 (R.A. = 22^{h}35^{m}58.^{s}6, decl. = +33^{d}58^{m}56.^{s}0, v = 6881 km s^{-1}) and #131 (R.A. = 22^{h}35^{m}58.^{s}6, decl. = +33^{d}58^{m}54.^{s}4, v = 6856 km s^{-1}) of S. Duarte Puertas et al. (2019), both having broad Hα lines and line ratios consistent with shock excitation (S. Duarte Puertas et al. 2019, 2021). The 15 μm emission associated with them must be unrelated to SF.

4.2. Dynamical Properties of Clumps

The left panel of Figure 6 shows the plot of velocity dispersion σ_v (Equation (A4)) versus the effective radius R_e (Equation (A5)) of the clumps. They have radii in the range 45–100 pc (with a mean of 72 ± 3 pc) and velocity dispersions in the range 2–20 km s^{-1} (mean = 7.4 ± 0.5 km s^{-1}). It is worth noting that quite a few clumps have sizes (= 2 × R_e) smaller than the spatial resolution of the ALMA observation (∼120 pc). This is because R_e is derived from an effective area A_e, which in turn is a flux-weighted summary of all pixels in a clump (Equation (A6)). The radius so defined has the advantage of being insensitive to the clump selection effects, but it is vulnerable to the error of the flux (similar to the error in measurement of the beam size using a point-source image). For faint clumps with $f_{CO21} \leqslant 0.03$ Jy km s^{-1}, corresponding to $\log(M_{mol}/M_{\odot}) \leqslant 5.7$, the error of R_e is of the order of 25%.

There is no significant difference in either R_e or σ_v between the three components. When compared with the clouds in the Milky Way disk (M. Heyer et al. 2009), the SQ-A clumps are in the regime of very large giant molecular clouds (GMCs). Indeed they fall right on the line of the so-called "Larson law" (the solid line in the plot) found for the Galactic GMCs (P. M. Solomon et al. 1987). On the other hand, the clouds in the overlap region of the Antennae Galaxies (hereafter the Antennae overlap) have significantly higher velocity dispersions, ∼5× above those of SQ-A clumps and clouds in the Milky Way disk, indicating different physical conditions in them (G. Krahm et al. 2024).

The right panel of Figure 6 is a plot of the external pressure P_e (Equation (A19)) versus the virial parameter α_{vir} (Equation (A20)). Here again the clumps in different kinematic components are well mixed with each other. All but two of them have $\alpha_{vir} > 2$, i.e., are unbound by gravity. P_e/k_B is in the range 3×10^3–10^6 K cm^{-3}, significantly lower than that of clumps in the Antennae overlap (G. Krahm et al. 2024). Rather, P_e/k_B of SQ-A clumps is similar to that of the GMCs in the Milky Way and nearby galaxies (M. Heyer et al. 2009; D. Donovan Meyer et al. 2013). Note that adopting a higher CO conversion factor would increase the value of P_e/k_B and reduce the value of α_{vir}. There is a strong correlation between P_e/k_B and α_{vir} (the Spearman correlation coefficient $r_s = 0.62$ with a significance of $p = 6 \times 10^{-5}$), indicating that the clumps are mainly confined by the external pressure instead of self-gravity. The clouds in the Antennae overlap, which have much higher P_e/k_B and α_{vir} values, lie slightly (by ∼0.5 dex) above this correlation.

4.3. Star Formation Properties of Clumps

Figure 7 presents the Σ_{SFR} versus Σ_{mol} plot (the "Kennicutt–Schmidt plot") of the clumps. The solid line (with a slope of 1.4) in the figure represents the trend followed by galaxies (K. Alatalo et al. 2014) and the two dotted lines mark deviations by ±1 order of magnitude. Clumps of three different kinematic components have similar Σ_{mol} values. In contrast, their Σ_{SFR} values are stratified over a range of ∼2 orders of magnitude: 6600 clumps are on the top, 6000 clumps in the middle, and 6900 clumps at the bottom. The high SFR enhancement of 6600 clumps is consistent with the nature of the SQ-A starburst, which is associated with this kinematic component. The 6000 clumps are also undergoing active SF, while most of 6900 clumps are clearly suppressed with Σ_{SFR} about an order of magnitude lower than the nominal line. In SQ-A clumps, Σ_{SFR} does not depend on Σ_{mol} at all: their Spearman rank correlation coefficient is $r_s = -0.04$ and the significance parameter (i.e., probability of the null hypothesis) $p = 0.82$.

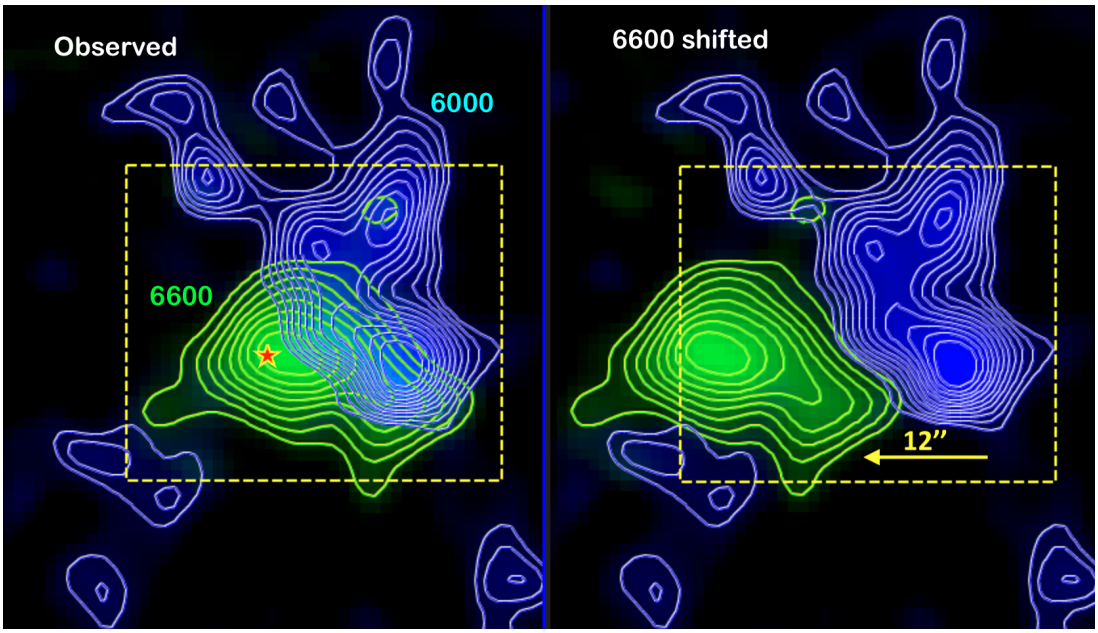

Figure 4. Left: H I maps in the SQ-A region. The blue and green colors are for the 6000 and 6600 components, respectively. The contour levels are 0.04, 0.05, 0.06, … Jy beam^{-1} km s^{-1}. The red star shows the location of the SQ-A starburst (redshift: 6680 km s^{-1}, S. Duarte Puertas et al. 2019). Right: same as the left panel except that the map of the 6600 component is shifted eastward by 12″.

The depletion timescale $t_{\rm dep}$, the inverse of the SFR per unit $M_{\rm mol}$, is another SF activity indicator. Compared to $\Sigma_{\rm SFR}$, $t_{\rm dep}$ has the advantage of being an intensive physical property and therefore insensitive to the "rich man effect" (large clouds having a large amount of everything). Figure 8(a) presents a plot of $t_{\rm dep}$ versus the virial parameter $\alpha_{\rm vir}$. There is no significant correlation between these two variables—further evidence for self-gravity not playing an important role in regulating the SF activity of the clumps. On the other hand, there is a marginally significant correlation between $t_{\rm dep}$ and the velocity dispersion σ_v (the significance parameter $p = 0.02$, Figure 8(b)). Given the fact that the clumps have σ_v much larger than the sound speed ($v_{\rm sound} \sim 0.2$ km s^{-1} for gas of $T \sim 10$ K) and therefore are dominated by nonthermal motions, the correlation suggests that the gas motion may play a significant role affecting the SF activity in the clumps.

The nonthermal motions can be in many different forms, including contraction, expansion, rotation, shear, and small-scale turbulent motions. Together with the thermal motion, they form a hierarchy and the energy cascades down from large scales to small scales. In collision systems, the main energy source is the shock triggered by collision (P. Guillard et al. 2009, 2022). With a resolution of ∼120 pc, we cannot resolve the small-scale turbulence. Therefore we begin by checking the effects of rotation and shear on $t_{\rm dep}$. A plot of $t_{\rm dep}$ versus the S parameter (Equation (A7)) is presented in Figure 8(c). Being a measure of the specific angular momentum, the S parameter is related to a centrifugal force that can balance gravity and suppress the SF. Indeed we see a significant correlation between $t_{\rm dep}$ and S with a Spearman correlation coefficient of $r_s = 0.50$ and a significance of $p = 2 \times 10^{-3}$. There is a trend that a kinematic component with longer average $t_{\rm dep}$ (i.e., low SF activity) has also a higher average S value ($\langle \log(S) \rangle = 1.96 \pm 0.19, 2.13 \pm 0.13$, and 2.19 ± 0.10 for the 6600, 6000, and 6900 components, respectively). The S-values have large scatters within individual components and the clear dependence of $t_{\rm dep}$ on S can be recognized in each of the three components. It should also be noted that the $t_{\rm dep}$ versus S plot is still stratified in the sense that, for a given S, the 6900 clumps tend to have long $t_{\rm dep}$ and the 6600 clumps short $t_{\rm dep}$, and the 6000 clumps are in between. This indicates that some other factors, which may be systematically different in the different kinematic components, can significantly affect the SF in clumps. J. Braine et al. (2018, 2020) found a

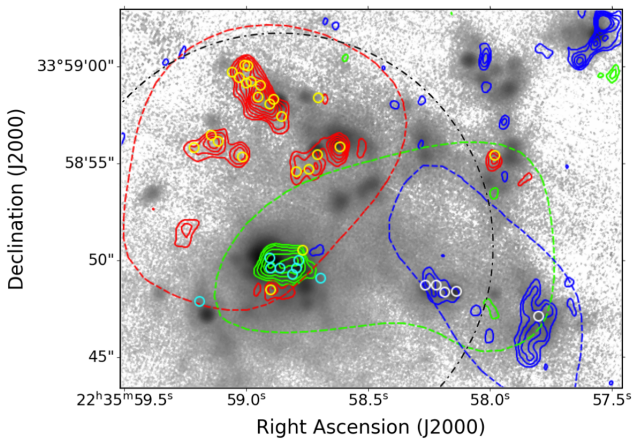

Figure 5. Contour maps of the CO(2–1) emissions overlaid on a JWST 15 μm image. Solid contours are for the combined TM2+ACA data, which have a synthetic beam of 1.″0 × 0.″66, with the blue contours representing the 6000 component (levels: 0.14, 0.19, 0.24, 0.29, and 0.34 Jy beam^{-1} km s^{-1}), the green contours the 6600 component (levels of 0.16, 0.2, 0.25, 0.3, and 0.35 Jy beam^{-1} km s^{-1}), and the red contours the 6900 component (levels of 0.22, 0.27, 0.32, and 0.37, … Jy beam^{-1} km s^{-1}). These maps have rms of 0.048, 0.053, and 0.059 Jy beam^{-1} km s^{-1}, respectively. Dashed contours (just one level at 1.3 Jy beam^{-1} km s^{-1}) are for the ACA data, which have a synthetic beam of 8.″0 × 7.″0; again the blue, green, and red contours are for the 6000, 6600, and 6900 components, respectively. The small circles ($r = 0.''25$) represent the clumps identified in Field 4 of the high-resolution CO(2–1) observations (beam = 0.″38 × 0.″23), with the colors white, cyan, and yellow representing the 6000, 6600, and 6900 components, respectively. The black dashed–dotted line marks the boundary of the primary beam ($r = 11''$) of the high-resolution CO(2–1) single-pointing observation.

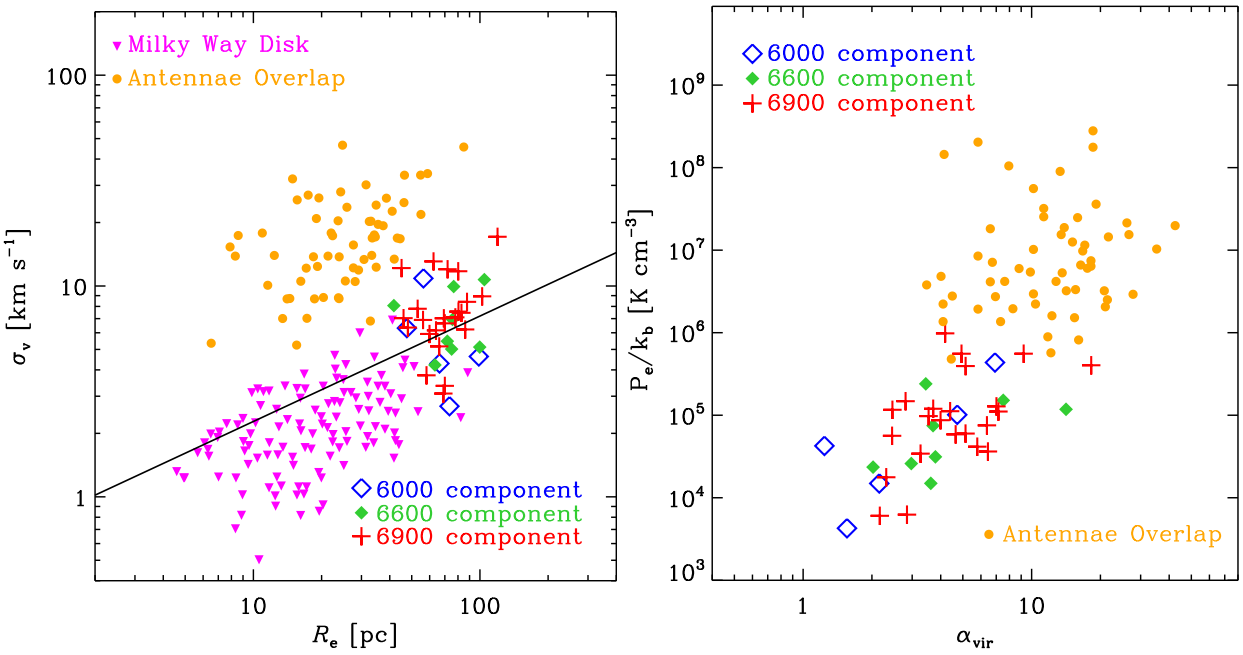

Figure 6. Left: plot of σ_v vs. R_e for clumps the in SQ-A region, compared with the clumps in the Antennae overlap (G. Krahm et al. 2024) and clouds in the Milky Way disk (M. Heyer et al. 2009). The solid line shows the typical relation for Galactic GMCs (P. M. Solomon et al. 1987). Right: P_e vs. α_{vir} plot of clumps in the SQ-A region, where P_e is the external pressure and α_{vir} the virial parameter. The yellow dots represent clumps in the Antennae overlap (G. Krahm et al. 2024).

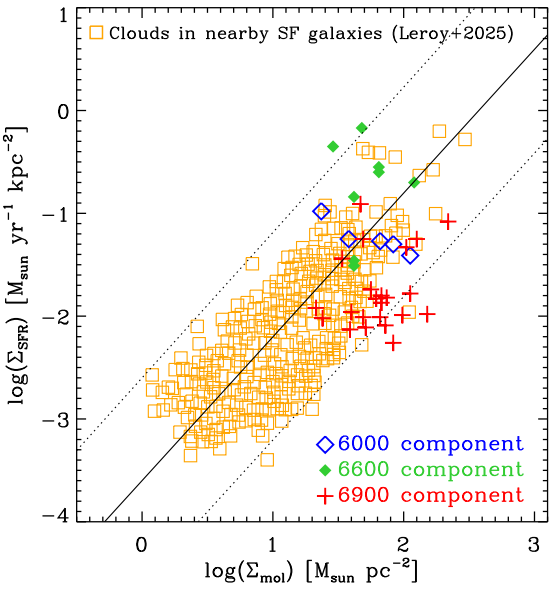

Figure 7. Kennicutt–Schmidt plot of the clumps in the SQ-A region, compared with molecular clouds in some nearby SF galaxies (A. K. Leroy et al. 2025). The solid line (with a slope of 1.4) represents the trend followed by galaxies (K. Alatalo et al. 2014) and the two dotted lines mark deviations by ±1 order of magnitude.

tendency for rotation vectors of molecular clouds in M33 and M51 to align with the galactic disk rotation. However, for SQ-A clumps no trend is found for the orientation of the 2D vector ***S*** (Figure 8(e)). This is consistent with the rotation being driven by localized torques (presumably associated with the collision) instead of effects associated with large-scale motions (as in the cases of M33 and M51 clouds).

Local torque can be generated by shear motion inside the clump, which in turn can be powered by a shock (particularly an oblique shock). The amplitude of a shear can be measured by velocity gradient. Figure 8(d) presents a plot of t_{dep} versus the radial velocity gradient G_v (Equation (A14)), which shows no significant correlation between the two variables. This suggests that shear motion may not have a significant direct impact on the SFR.

Figure 8(f) presents a plot of t_{dep} versus the C parameter, the ratio of nonrotational to rotational energy (Equation (A10)). There is a significant anticorrelation in this plot, with a Spearman correlation coefficient of $r_s = -0.41$ and significance $p = 0.01$. Here we see an even better separation in C than in the S parameter between the three kinematic components: on average the 6600 component has the highest C and shortest t_{dep} and the 6900 component the lowest C and longest t_{dep}. While the correlation between t_{dep} and the S parameter indicates a role of rotation in suppressing the SFR, the anticorrelation between t_{dep} and the C parameter suggests a positive role for nonrotational motion in enhancing the SFR. Simulations have shown that collisions can generate compressive turbulence (K. Takahira et al. 2014), which in turn can enhance the SFR (M. R. Krumholz 2014; F. Renaud et al. 2014). It is plausible that the compressive turbulence, which is included in the nonrotational motion, is the engine that drives the enhanced SFR.

By measuring the rotational support and nonrotational motions at cloud scale, we can estimate the degree of stability of the molecular structures, and connect it to the SF activity. However, this reasoning is not sufficient to explain the starburst nature of these regions, which is why SF proceeds faster here than in classical clouds with the same mass of molecular gas. F. Renaud et al. (2014) used simulations of interacting galaxies to establish that the starburst regime is reached when the interstellar turbulence becomes dominantly compressive (as opposed to solenoidal) as the result of galactic-scale tidal compression. This induces an excess of dense gas, which not only allows for elevated star formation (high SFR) but also fast SF (short depletion time). The same

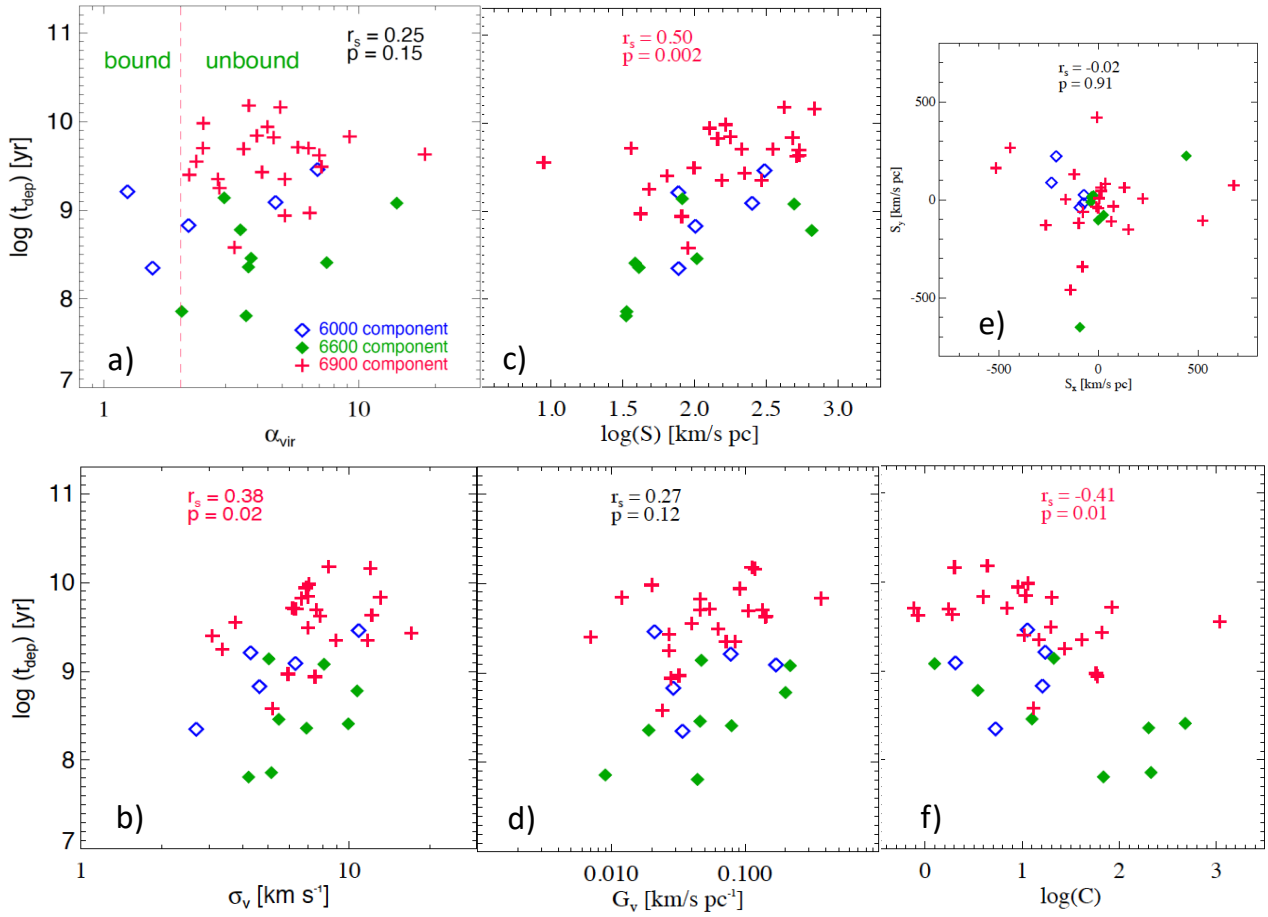

Figure 8. (a) Plot of depletion time (t_{dep}) vs. virial parameter (α_{vir}). The red dashed vertical line at $\alpha_{vir} = 2$ marks the boundary separating gravitationally bound and unbound clumps. (b) Plot of t_{dep} vs. the velocity dispersion (σ_v). (c) Plot of t_{dep} vs. S parameter (the absolute value of the projected specific angular momentum vector $\boldsymbol{S}$). (d) Plot of t_{dep} vs. the radial velocity gradient (G_v). (e) Plot of S_y (the y-component of the projected specific angular momentum vector $\boldsymbol{S}$) vs. S_x (the x-component of the vector). It shows no trend for a preferred orientation of the vector. (f) Plot of t_{dep} vs. C parameter (the ratio of nonrotational to rotational energy). The Spearman rank correlation coefficient r_s and the significance parameter p (the probability of the null hypothesis) are listed in each plot, with red characters indicating significant ($p \leqslant 0.01$) or marginally significant correlations ($0.01 < p \leqslant 0.03$).

effect could well be active in SQ-A, with compression originating from the interaction between the intruder-associated material and the IGrM, and its energy being converted to compressive turbulence, in turn triggering the observed starburst. While our result on the anticorrelation between t_{dep} and the C parameter seems to support this hypothesis, it is important to note that we do not have any direct measure of the turbulent motion. Indeed, the ultimate test of this hypothesis would require the measurement of turbulent motions within the clouds themselves, which remains out of reach of the present capacities.

It should also be noted that all the correlations presented in Figure 8 are quite scattered even when they are significant ($p \leqslant 0.01$) or marginally significant ($0.01 < p \leqslant 0.03$). Although there is a trend that clumps in the more SF-active component tend to have lower S parameters and higher C parameters (e.g., $\langle \log(S) \rangle = 1.96 \pm 0.19$ and $\langle \log(C) \rangle = 1.53 \pm 0.32$ for those in the 6600 component), the differences with those in less SF-active components (e.g., in the 6900 component $\langle \log(S) \rangle = 2.19 \pm 0.10$ and $\langle \log(C) \rangle = 1.09 \pm 0.15$) are only at 1σ level between the corresponding means. The large scatters within the same kinematic component are understandable because many factors that are not controlled in this analysis can affect the variables. These include the variation of the evolution stages among the clumps, which strongly affects the estimate of t_{dep} (J. M. D. Kruijssen et al. 2018; J. Kim et al. 2022). Projection and beam smearing can affect many parameters such as R_e, σ_v, the S parameter (projected specific angular momentum), the C parameter (ratio of nonrotational to rotational energy), and the velocity gradient (G_v parameter). The small-scale variation of the CO conversion factor, particularly if it depends on t_{dep} (F. Renaud et al. 2019), can also add on to the scattering of t_{dep} significantly. Nevertheless, the correlations and noncorrelations between t_{dep} and various parameters may provide important insights to the factors that control the SF activity at the cloud level. In particular the significant correlation between S and t_{dep} strongly suggests that the rotation may play an important role in hindering collapse and suppressing the SFR. At the same time, our finding that the t_{dep} distribution is still stratified among different components for a given S (Figure 8(c)) demands other factors that can affect the triggered SF in clumps, such as the compression of gas hinted at by the significant anticorrelation between C and t_{dep}.

5. Discussion

5.1. CCC Model and SQ-A Starburst

Figures 3 and 4 provide new supporting evidence for the hypothesis that the SQ-A starburst is triggered by a collision between two gas systems, one associated with the IGrM ($v \sim 6900\,\mathrm{km\,s^{-1}}$) and another with the intruder galaxy NGC 7318b ($v \sim 6000\,\mathrm{km\,s^{-1}}$). Here we discuss this hypothesis in the context of the CCC theory. Originally, the CCC theory was proposed to interpret the triggered SF in Galactic GMCs, particularly the formation of young massive star clusters (YMCs; A. Habe & K. Ohta 1992; T. Inoue & Y. Fukui 2013; K. Takahira et al. 2014). More recently, this theory was applied to starbursts in large extragalactic regions (size up to a few kiloparsecs) involved in galaxy–galaxy collisions, such as the overlap region of the Antennae Galaxies (K. Tsuge et al. 2021a, 2021b) and 30 Doradus plus the southern ridge of the LMC (Y. Fukui et al. 2017; K. Tsuge et al. 2024). Similar to SQ-A, the Antennae overlap region is undergoing high SF enhancement due to a direct collision of two gas systems each associated with one galaxy (B. C. Whitmore & F. Schweizer 1995; C. Xu et al. 2000). However, there are remarkable differences between the two cases. As shown in Table 1, the kinematic systems in SQ-A are dominated by the H I gas (ratio $M_{\rm HI}/M_{\rm mol} \sim 10$). And the complementary distributions among the different components are found only in the H I maps, not in the CO maps (Figure 3). On the other hand, the collision in the Antennae overlap is happening primarily in the molecular gas, which is much more massive than the H I (C. D. Wilson et al. 2000; J. E. Hibbard et al. 2001), and the complementary distributions of the colliding systems are found in the CO maps (K. Tsuge et al. 2021a). Also, clouds in the Antennae overlap have much higher velocity dispersions and external pressures, $\sim 5\times$ and about two orders of magnitude higher than those in SQ-A clumps, respectively (right panel of Figure 6). Since the collision velocity in SQ-A is much higher than that in the Antennae overlap, which is $\sim 100\,\mathrm{km\,s^{-1}}$ (K. Tsuge et al. 2021a), the low pressure in the former is suggestive of a much lower pre-collision density than in the latter, given the relation $P_e \sim \rho_{\rm pre} v_{\rm coll}^2$ where $\rho_{\rm pre}$ is the pre-collision density and $v_{\rm coll}$ the collision velocity.

Indeed, SQ-A may be more comparable to the giant SF regions in 30 Doradus, which are produced presumably by a collision of two H I systems, one associated with the LMC and the other accreted from the SMC (Y. Fukui et al. 2017; K. Tsuge et al. 2024). It is worth noting that, similar to the LMC, SQ-A has a subsolar metallicity of $Z \sim 0.5\,Z_\odot$ (S. Duarte Puertas et al. 2021), which might be the reason for its high $M_{\rm HI}$-to-$M_{\rm mol}$ ratio. In direct GMC–GMC collisions, SF is triggered in the denser and smaller cloud when it crashes into a less dense and larger cloud (A. Habe & K. Ohta 1992; Y. Fukui et al. 2018). On the other hand, the triggered SF in H I–H I collisions is different. As shown in the simulations of R. Maeda et al. (2021, 2024), high-velocity collisions ($v_c \gtrsim 50\,\mathrm{km\,s^{-1}}$) of H I gas can trigger the formation of a large number of dense cores (density $>10^4\,\mathrm{cm^{-3}}$), which in turn form YMCs on a short timescale comparable to the freefall time of the dense cores ($t_{\rm ff} \lesssim 10^6$ yr). In these models, because of the rapid cooling ($t_{\rm cool} < 10^6$ yr), the density of the postshock gas is approximately proportional to the shock velocity, which is about half of the collision velocity. Assuming a collision velocity of $\sim 1000\,\mathrm{km\,s^{-1}}$ (as it is in SQ-A) and an initial density of $n_0 = 1\,\mathrm{cm^{-3}}$, the postshock gas density becomes as high as $n \sim 350\,\mathrm{cm^{-3}}$ (R. Maeda et al. 2024). This gas is thermally unstable and has a freefall timescale of $t_{\rm ff} \sim 2 \times 10^6\,\mathrm{yr} \times (n/350\,\mathrm{cm^{-3}})^{-0.5}$. After a few $t_{\rm ff}$ dense cores will form and the starburst follows. The whole process should occur within a timescale of 10^7 yr, consistent with the timescale we found for the collision in SQ-A. Results of the clump analysis in Section 4, which shows a lack of dependence of SFR on density (Figure 7) and an anticorrelation between $t_{\rm dep}$ and the C parameter (Figure 8(f)), also support the scenario in which much of the SF in SQ-A is collisionally triggered instead of gravitationally induced. S. C. Gallagher et al. (2001) and K. Fedotov et al. (2011) found a large number of young stellar clusters (ages of $\leqslant 10^7$ yr) in SQ-A—further supporting evidence for collisionally triggered SF in the region given the tight relation between young clusters and CCC (Y. Fukui et al. 2021). Finally, although in SQ-A the CCC mainly occurs between H I-dominated clouds (i.e., H I–H I collisions), H I–GMC and GMC–GMC collisions may also contribute to the SF enhancement, albeit with relatively low significance given the low ratio $M_{\rm mol}/M_{\rm HI}$.

5.2. Collision of Clouds with Diffuse Gas and Suppression of SFR

A major challenge for the collisional scenario of the SQ-A starburst is the severely suppressed SF activity in the large-scale shock region (M. E. Cluver et al. 2010; P. Guillard et al. 2012). Why does a high-speed collision cause SF suppression in the large-scale shock region but a starburst in SQ-A?

There is a stark difference between the collisions in the two regions: in SQ-A both the IGrM and the intruder-associated components have a large amount of cold gas. On the other hand, in the shock region, only the molecular CO gas of the intruder-associated component (i.e., the 6000 component) is significantly detected (U. Lisenfeld et al. 2002; P. Guillard et al. 2012; B. H. C. Emonts et al. 2025) whereas no significant CO or H I detection is found for the IGrM-associated component. J. W. Sulentic et al. (2001) suggested that the reason for the lack of cold IGrM gas in the shock region is because it has been converted to hot X-ray gas and warm ionized gas after the collision. This interpretation is unlikely to be true because, as shown in simulations (e.g., R. Maeda et al. 2021), the cooling time in cloud–cloud collisions is so short that the postshock gas becomes cold and neutral again soon after collision (on a timescale of $<10^6$ yr). It is more likely that the preshock IGrM in the shock region is predominantly in the diffuse warm neutral medium (WNM) or/and the warm ionized medium (J. Iglesias-Páramo et al. 2012; M. Rodríguez-Baras et al. 2014; M. I. Arnaudova et al. 2024). The WNM gas is too diffuse to be detected by the VLA but can be picked up by sensitive single-dish H I observations. Indeed recent FAST observations of SQ have found more H I gas in the 6600 components, most likely in the diffuse IGrM (C. K. Xu et al. 2022; C. Cheng et al. 2023). If indeed the preshock IGrM gas in the shock region is diffuse and of low density, the high-speed collision between this gas and the diffuse gas associated with the intruder can produce two large shock fronts: one propagates in the IGrM and the other in the system associated with the intruder. The shock ridge shown in the X-ray and the radio continuum is presumably associated with the postshock gas between these two shock fronts. From the X-ray data

G. Trinchieri et al. (2003) found a preshock gas density of the order of $\sim 10^{-2}\,\mathrm{cm}^{-3}$. Therefore, the process affecting the clouds in the shock region may be better analyzed using models for interaction of a blast-wave shock and interstellar clouds (C. F. McKee & L. L. Kowie 1975; R. Klein et al. 1994; P. Guillard et al. 2009) instead of CCC models. One of the key findings of R. Klein et al. (1994) is that strong vorticity can be generated at the cloud–intercloud boundary and in the tail behind the cloud, both by the initial passage of the blast-wave shock and by the subsequent flow of postshock intercloud gas passing by the cloud. We argue that it is the vortices so generated that suppress the SF in molecular clouds in the shock region. The vortices can contribute significantly to the solenoidal turbulence, which acts against cloud contraction, and may eventually destroy the cloud (R. Klein et al. 1994). Both theoretical simulations and observations in the literature have shown that, while the compressive turbulence can enhance the SFR, the solenoidal turbulence can suppress it (C. Federrath & R. S. Klessen 2012; J. H. Orkisz et al. 2017; R. Rani et al. 2022; M. A. Petkova et al. 2023).

Similar to clouds in the shock region, clumps of the 6900 component in SQ-A have severely suppressed SF activity. It is possible that these clumps have avoided cloud–cloud collision, given the fact that they have not been decelerated significantly. If these clumps are also undergoing interactions with high-speed shocks due to collisions between diffuse media in SQ-A, the above scenario proposed for clouds in the shock region can apply and can explain why the SFR is suppressed in the 6900 component. The significant correlation between $t_{\rm dep}$ and the S parameter, which indicates an important role of rotation in suppressing SFR, supports this hypothesis. The weak X-ray emission in SQ-A may not be used as evidence against such an analogy because the X-ray emission may be affected by absorption (E. O'Sullivan et al. 2009). It is interesting to note that there is a faint stripe of diffuse X-ray emission extending to the east of SQ-A (E. O'Sullivan et al. 2009), which can also be seen in the VLA 1.4 GHz radio continuum map (C. K. Xu et al. 2003) and is faintly visible in the Hα map (Figure 1). This feature may be shock-excited, providing further evidence for shocks triggered by the collision between diffuse media in the region around SQ-A.

Unlike the 6000 component, which is linked to the intruder galaxy NGC 7318b by a long arm or a partial ring (B. H. C. Emonts et al. 2025), the origin of the 6900 component in SQ-A is still unknown. It might be related to the large CO emission region in the north of the nucleus of NGC 7319, which has a systemic velocity of $\sim 6900\,\mathrm{km\,s}^{-1}$ (M. S. Yun et al. 1997; Y. Gao & C. Xu 2000; B. H. C. Emonts et al. 2025), though no clear link has been detected between that region and SQ-A in any band. Future high-angular-resolution and high-sensitivity H I observations covering the velocity range beyond $6800\,\mathrm{km\,s}^{-1}$ will help to resolve this issue.

Our interpretation for the diversified $t_{\rm dep}$ in colliding systems in SQ can have far-reaching implications for theories of interaction-induced SF in galaxy mergers, particularly those in early merging stages (e.g., optical–NIR-selected pairs). Given the nearly universal detections of YMCs in merging galaxies (B. C. Whitmore & F. Schweizer 1995; A. Adamo et al. 2020) and the tight relation between YMCs and collision-triggered SF (B. G. Elmegreen 1998; Y. Fukui et al. 2021), the CCC mechanism must play an important role in the SF activity of galaxy mergers. Our results for SQ-A indicate that the effects of collisions are very complex, and can cause either SF enhancement or SF suppression depending on the density contrast between the gas systems involved in the collision. In studies of a sample of K-band-selected close major-merger pairs (KPAIR), it has been found that the SF galaxies in spiral–spiral pairs have strong SF enhancement while those in spiral–elliptical mixed pairs do not (C. K. Xu et al. 2010; C. Cao et al. 2016; U. Lisenfeld et al. 2019). Simulations predict enhancement of compressive turbulence in early mergers (F. Renaud et al. 2014), which triggers the formation of a large number of dense cores and results in widely spread SF enhancement in the disks, consistent with the observations of extended SF enhancement in disks in spiral–spiral pairs (D. Iono et al. 2005). Why does this mechanism fail to work for SF galaxies in mixed pairs? C. K. Xu et al. (2021) found that galaxies in mixed pairs are more likely to be involved in high-inclination orbits and high-speed collisions, which may trigger density waves (as shown by ring-like structures) in the disk. It is plausible that the shocks associated with density waves may act similarly to the blast-wave shock in the model of R. Klein et al. (1994) and suppress the SF of the gas clouds. As an example, $\mathrm{SFR}/M_{\rm mol}$ (the inverse of $t_{\rm dep}$) of the spiral galaxy NGC 2936 in the mixed pair Arp 142, which has gone through a high-speed and high-inclination collision recently, is significantly lower than the nominal value for SF regions (C. K. Xu et al. 2021).

5.3. Uncertainties of CO Conversion Factor and r_{21}

In this paper, we adopt a CO conversion factor $\alpha_{\rm CO10} = 1.0\,M_\odot\,(\mathrm{K\,km\,s^{-1}\,pc^2})^{-1}$. This is a factor of 3.2 or 4.3 lower than the Galactic value, depending on whether the contribution of heavy elements is included (A. D. Bolatto et al. 2013). Starburst galaxies often have low CO conversion factors ($\alpha_{\rm CO10} < 1$; D. Downes & P. M. Solomon 1998). There is also evidence for molecular gas systems involved in high-speed collisions having low $\alpha_{\rm CO10}$. For gas in the bridge between the Taffy Galaxies, J. Braine et al. (2003) and M. Zhu et al. (2007) found a $\alpha_{\rm CO10}$ 4–10 times lower than the Galactic value. Given that SQ-A is also involved in a high-speed collision with a collision velocity comparable to that between the Taffy Galaxies, the low $\alpha_{\rm CO10}$ is justified. On the other hand, the slightly subsolar metallicity of SQ-A ($Z \sim 0.5\,Z_\odot$, S. Duarte Puertas et al. 2021) may suggest a higher $\alpha_{\rm CO10}$ (A. D. Bolatto et al. 2013). Also, the average virial parameter of the SQ-A clumps is $\alpha_{\rm vir} \sim 3$ (see right panel of Figure 6), indicating that the virial mass is about three times higher than the mass estimated using the adopted $\alpha_{\rm CO10}$. However, in colliding systems and starbursts, the virial equilibrium may be broken and virial mass may not be a good estimator of the true mass. Constraining $M_{\rm mol}$ using the local thermodynamic equilibrium (LTE) models, G. Krahm et al. (2024) found that the conversion factor in the Antennae overlap is consistent with $X_{\rm CO} = 0.5 \times 10^{20}\,\mathrm{cm^{-2}}\,(\mathrm{K\,km\,s^{-1}})^{-1}$, corresponding to $\alpha_{\rm CO10} = 1.075\,M_\odot\,(\mathrm{K\,km\,s^{-1}\,pc^2})^{-1}$ (A. D. Bolatto et al. 2013), and that the clouds in the Antennae overlap are highly supervirial with a mean $\alpha_{\rm vir} = 13.77 \pm 0.37$. Actually, these authors found that molecular clouds are in general supervirial in starburst galaxies. In summary, the CO conversion factor in SQ-A is highly uncertain. Future works involving ^{13}CO observations and modelings, e.g., using the LTE models or

models with a large velocity gradient (A. D. Bolatto et al. 2013), may help to resolve this issue.

Also, the adopted CO(2–1) to CO(1–0) luminosity ratio $r_{21} = 0.34$ is quite uncertain, too, because SQ-A is near the edge of the primary beam of the CARMA CO(1–0) observations on which the estimate of the r_{21} value is based. In addition, the 6000 component (associated with the intruder) may have a slightly different value ($r_{21} = 0.29$; B. H. C. Emonts et al. 2025).

The uncertainties of $\alpha_{\rm CO10}$ and r_{21} affect the estimate of $M_{\rm mol}$ from the ALMA CO(2–1) data through a combined factor $\alpha_{\rm CO10} \times r_{21}$. Nevertheless our main conclusions, which are primarily based on gas distributions and correlations (and the lack of them) between various parameters in clumps, are not significantly affected by these uncertainties.

6. Conclusions

In this paper we aim to achieve two science goals: (1) proving the validity of the hypothesis that the starburst SQ-A in the IGrM of SQ is triggered by a high-speed collision ($\sim$900 km s^{-1}) between two gas systems, one associated with the IGrM ($v \sim 6900$ km s^{-1}) and the other with the intruder galaxy NGC 7318b ($v \sim 6000$ km s^{-1}); (2) solving the puzzle of why gas clouds in SQ-A and in the large-scale shock region of SQ, which are both involved in the same high-speed collision between the IGrM and the intruder, can have dramatically different SFRs. To achieve these goals, we exploit the following data sets: (1) CO(2–1) data cubes with angular resolutions in the range 0.″2–7.″0 obtained using ALMA in various configurations (with the adopted distance of 94 Mpc, 1″ corresponds to 0.45 kpc); (2) an H I data cube of angular resolution 6.″6 × 7.″9 obtained using the VLA B, C, and D arrays; and (3) a JWST MIRI image in the 15 μm band. We reach the following conclusions.

1. The CO(2–1) data show clearly three kinematic systems in SQ-A that correspond to the 6000, 6600, and 6900 components in the literature (G. S. Shostak et al. 1984; B. A. Williams et al. 2002; C. Cheng et al. 2023), with systematic velocities of 6010 ± 32, 6719 ± 41, and 6930 ± 33 km s^{-1}, respectively. As shown in the CO maps covering the entire SQ (B. H. C. Emonts et al. 2025), both the 6600 and 6900 components in SQ-A are most likely associated with the IGrM and the 6000 component with the intruder galaxy NGC 7318b. The 6900 component has the highest molecular gas mass ($M_{\rm mol} = (1.4 \pm 0.7) \times 10^8\ M_\odot$), which is 1.9 and 1.5 times those of the 6000 and 6600 components, respectively. The 6900 and 6000 components do not overlap with each other spatially but are bridged by the 6600 component.
2. The 6000 and 6600 components are also detected in new H I data with velocities of 6020 ± 31 and 6645 ± 63 km s^{-1}, respectively, slightly different from those of the corresponding components in the CO. The 6900 component is not observed in H I because it is outside the frequency coverage of the VLA observations. Both the 6000 and 6600 components show rather high $M_{\rm HI}$-to-$M_{\rm mol}$ ratios (>10). A comparison with an unpublished MeerKat H I observation indicates a lower $M_{\rm HI}$-to-$M_{\rm mol}$ ratio for the 6900 component ($\sim$4). In the H I map the 6600 component fits well into a gap in the more extended 6000 component, albeit with a displacement of $\sim$5 kpc.
3. The three kinematic components in SQ-A have very different SF activities. The 6600 component has the highest SFR (0.98 $M_\odot$ yr^{-1}), dominated by the starburst ($v \sim 6680$ km s^{-1} in Hα). The 6000 component has also a sizable SFR though about a factor of 3 lower than that of the 6600 component. The 6900 component has very little SF, with an SFR more than an order of magnitude lower than that of the 6600 component.
4. In order to probe at the cloud level the physical conditions that lead to the conspicuous difference in SFRs of different kinematic components, we carry out an analysis of CO clumps of sizes $\sim$100–200 pc, utilizing the high-resolution ALMA data (beam =0.″38 × 0.″23) and the clump-finding algorithm "Fellwalker" (D. Berry 2015). The Larson relation between the effective size (R_e) and the velocity dispersion (σ_v) of these clumps is similar to that of the large Galactic GMCs. No significant systematic difference is found among the different kinematic components in various physical parameters including R_e, σ_v, the virial parameter $\alpha_{\rm vir}$, and the external pressure P_e.
5. Correlation analyses of the clumps find no dependence of the SFR surface density $\Sigma_{\rm SFR}$ and the depletion time of molecular gas $t_{\rm dep}$ on molecular gas surface density $\Sigma_{\rm mol}$ nor on the virial parameter $\alpha_{\rm vir}$, suggesting that the SFR enhancement (or suppression) is not due to any mechanism associated with self-gravity. On the other hand, a marginally significant correlation is found between $t_{\rm dep}$ and σ_v, suggesting that the gas motion may play a role in the SF activity of the clumps. Additional correlation analyses find putatively significant correlation between $t_{\rm dep}$ and the S parameter (a measure of projected angular momentum) and anticorrelation between $t_{\rm dep}$ and the C parameter (a measure of the ratio of nonrotational to rotational energy), suggesting that SFR may be suppressed by the centrifugal force in clumps with strong rotation and enhanced by compressive processes in clumps with a high ratio of nonrotational to rotational energy. No correlation is found between $t_{\rm dep}$ and the radial velocity gradient parameter G_v, suggesting the shear motion may not affect the SFR significantly.
6. In analogy to the SF enhancement in 30 Doradus plus the southern ridge of the LMC (K. Tsuge et al. 2024), the following scenario for the triggering of the SQ-A starburst is supported by our results: A high-speed collision ($v_{\rm coll} \gtrsim 900$ km s^{-1}) is going on between the IGrM (pre-collision radial velocity $\sim$6900 km s^{-1}) and a gas system associated with the intruder galaxy NGC 7318b (pre-collision radial velocity $\sim$6000 km s^{-1}). Only a part of the 6900 component and a part of the 6000 component are involved in the collision. During the collision the 6900 gas, which is likely to be denser and more compact than the 6000 gas, is decelerated and compressed, and this decelerated and compressed gas becomes the 6600 component in which the SQ-A starburst is triggered. At the same time, the 6000 gas involved in the collision is swept into the 6600 component and/or dispersed, leaving a gap in the 6000

map at the place where the 6600 component crashes through. The ∼5 kpc displacement shown in Figure 4, which is likely the projection of a three-dimensional movement between the two components, suggests an age of the collision of a few 10^7 yr (assuming a transverse relative velocity of a few hundred km s^{-1} between the colliding systems), consistent with the estimated timescale for the age of the encounter between the intruder and SQ (J. W. Sulentic et al. 2001). According to simulations of R. Maeda et al. (2021, 2024), the high $\Sigma_{\rm SFR}$ and short $t_{\rm dep}$ of clumps in the 6600 component (dominated by H I gas with an $M_{\rm HI}$-to-$M_{\rm mol}$ ratio > 10) are due to strong compression in the post-collision gas, which triggers the formation of a large number of star-forming dense cores ($n > 10^4$ cm^{-3}).

7. Different from the clumps of the 6600 component in SQ-A, the molecular clouds in the large-scale shock region and in the 6900 component in SQ-A show severely suppressed SF activity. These clouds are likely not involved in any cloud–cloud collision but in more complex collisions involving dense clouds and low-density diffuse media. In this scenario, high-speed large shocks (as shown by the radio and X-ray ridge) are triggered by the collision between diffuse media associated with the IGrM and the intruder, respectively. As predicted by the model for interaction of a blast-wave shock and dense clouds (R. Klein et al. 1994), strong vorticity at the cloud–intercloud boundary and in the tail behind a dense cloud can be generated both by the initial passage of the high-speed shock and by the subsequent flow of postshock intercloud diffuse gas passing by the cloud. It is the vortices so generated that suppress the SF in the clouds with low SF activity.

Acknowledgments

We thank K. Rajpurohit for providing useful information from her MeerKAT observations before publication. This work is sponsored (in part) by the Chinese Academy of Sciences (CAS) through a grant to the CAS South America Center for Astronomy. C.C. acknowledges NSFC grants No. 11803044 and 12173045. This work is supported by the China Manned Space Program with grant No. CMS-CSST-2025-A07. U.L. acknowledges support by the research grants PID2020-114414GB-I00 and PID2023-150178NB-I00, financed by MCIU/AEI/10.13039/501100011033 and from the Junta de Andalucía (Spain) grant FQM108. P.A. and S.G. thank the Canadian Space Agency and the Natural Science and Engineering Council for support.

This paper makes use of the following ALMA data: ADS/JAO.ALMA#2015.1.00241.S and ADS/JAO.ALMA#2023.1.00177.S. ALMA is a partnership of ESO (representing its member states), NSF (USA) and NINS (Japan), together with NRC (Canada), MOST and ASIAA (Taiwan), and KASI (Republic of Korea), in cooperation with the Republic of Chile. The Joint ALMA Observatory is operated by ESO, AUI/NRAO and NAOJ. The National Radio Astronomy Observatory is a facility of the National Science Foundation operated under cooperative agreement by Associated Universities, Inc.

This work is based on observations made with the NASA/ESA/CSA James Webb Space Telescope. The data were obtained from the Mikulski Archive for Space Telescopes at the Space Telescope Science Institute, which is operated by the Association of Universities for Research in Astronomy, Inc., under NASA contract NAS 5-03127 for JWST.

Some of the data presented in this paper were obtained from the Mikulski Archive for Space Telescopes (MAST) at the Space Telescope Science Institute. The specific observations analyzed can be accessed via doi:10.17909/9w9c-f533. STScI is operated by the Association of Universities for Research in Astronomy, Inc., under NASA contract NAS5-26555. Support to MAST for these data is provided by the NASA Office of Space Science via grant NAG5-7584 and by other grants and contracts.

Some of the data products presented herein were retrieved from the Dawn JWST Archive (DJA). DJA is an initiative of the Cosmic Dawn Center (DAWN), which is funded by the Danish National Research Foundation under grant DNRF140.

Appendix
Clumps in Field 4

We identified clumps in the CO(2–1) data cube of the "Field 4" observation of P. N. Appleton et al. (2023) using the Fellwalker clump-finding algorithm via PyCupid,[22] which is a Python wrapper for the Starlink CUPID package (D. S. Berry et al. 2007; M. J. Currie et al. 2014). The detection parameters were configured as follows: a detection threshold of 1σ above the background level, a minimum clump peak height of 2σ (minheight = 2), a separation threshold of 1σ between adjacent clumps (mindip = 1), a maximum step of 8 pixels to search for a higher neighboring pixel value (maxjump = 8), and a minimum clump size (this size is measured using the sum of all pixels in the clump without the flux weight) of twice the synthesized beam size in pixel (minpix = 2 beam FWHM). These settings ensure detection of resolved, statistically significant structures while mitigating false positives in crowded molecular environments. Clumps composed of two or more subclumps spatially separated by gaps $\geqslant$5 pixels (1 pixel =0.″05) are excluded. In total 36 clumps are identified in the field. Table A1 lists various parameters of these clumps. The parameters for individual clumps are defined as follows.

The position (i.e., R.A. and decl.) of each clump is specified by that of its center of mass, whose x- and y-coordinates (in the image frame) are

$$x = \sum_i f_i x_i / \sum_i f_i \quad \text{(A1)}$$

$$y = \sum_i f_i y_i / \sum_i f_i, \quad \text{(A2)}$$

where x_i, y_i, and f_i are the coordinates and the signal of the ith pixel, respectively, and the summation goes through all pixels in the clump. The parameter $r_{\rm SQA}$ is the distance from a clump to the center of Field 4 (at R.A. = 338°.995333, decl. = +33°.98074), which is in the direction of the SQ-A starburst with a primary beam of 22″. Two clumps (#35 and #36) have $r_{\rm SQA} > 11''$ and therefore are outside the primary beam. They should be treated with caution. The redshift velocity v and the velocity dispersion σ_v of a given clump are estimated as follows:

$$v = \sum_i f_i v_i / \sum_i f_i, \quad \text{(A3)}$$

[22] https://github.com/msanchezc/pycupid

Table A1
Properties of Individual CO Clumps

ID	R.A. (J2000)	Decl. (J2000)	r_{SQA}[a] (arcsec)	v[b] (km s^{-1})	σ_v[c] (km s^{-1})	R_e[d] (pc)	f_{CO21}[e] (Jy km s^{-1})	log(M_{mol})[f] ($M_\odot$)	α_{vir}[g]	log(P_e/k_B)[h] (K cm^{-3})	log(Σ_{mol})[i] ($M_\odot$ pc^{-2})	log(S)[j] (km s^{-1} pc)	log(G_v)[k] (km s^{-1} pc^{-1})	log(C)[l]	log(Σ_{SFR})[m] ($M_\odot$ yr^{-1} kpc^{-2})	log(t_{dep})[n] (yr)
1	338.99552	+33.98058	0.81	6723	5.13	99.8	0.096	6.18	2.0	4.37	1.68	1.53	−2.05	2.33	−0.17	7.86
2	338.99535	+33.98044	1.11	6717	9.94	76.6	0.076	6.07	7.5	5.18	1.81	1.59	−1.10	2.68	−0.60	8.41
3	338.99496	+33.98070	1.11	6974	7.46	82.9	0.067	6.02	5.1	4.78	1.69	1.91	−1.55	1.77	−1.25	8.94
4	338.99503	+33.98055	1.13	6750	10.72	104.6	0.263	6.61	3.4	5.38	2.08	2.82	−0.70	0.54	−0.70	8.78
5	338.99551	+33.98044	1.22	6736	4.22	63.3	0.023	5.56	3.6	4.17	1.46	1.52	−1.36	1.84	−0.35	7.81
6	338.99507	+33.98044	1.37	6747	6.94	75.7	0.073	6.06	3.7	4.88	1.81	1.61	−1.72	2.30	−0.55	8.36
7	338.99513	+33.98035	1.54	6750	5.47	71.8	0.043	5.82	3.7	4.50	1.62	2.02	−1.34	1.10	−0.84	8.46
8	338.99551	+33.98013	2.30	6909	5.92	59.9	0.024	5.58	6.4	4.56	1.53	1.62	−1.49	1.76	−1.44	8.97
9	338.99466	+33.98030	2.58	6757	8.07	41.7	0.014	5.35	14.0	5.08	1.62	2.69	−0.66	0.10	−1.46	9.08
10	338.99507	+33.98181	3.92	6926	3.36	70.0	0.021	5.51	2.9	3.79	1.33	1.68	−1.57	1.44	−1.92	9.25
11	338.99486	+33.98186	4.23	6951	7.80	53.1	0.035	5.73	7.0	5.11	1.79	2.71	−0.85	−0.08	−1.83	9.62
12	338.99599	+33.98203	5.02	6957	6.16	64.0	0.032	5.69	5.7	4.62	1.59	1.56	−1.27	1.92	−2.13	9.71
13	338.99674	+33.97996	5.06	6665	5.02	75.0	0.047	5.87	3.0	4.41	1.62	1.91	−1.33	1.33	−1.51	9.14
14	338.99471	+33.98206	5.08	6949	11.75	80.2	0.161	6.40	5.2	5.59	2.10	2.19	−1.08	1.62	−1.25	9.35
15	338.99432	+33.98217	5.94	6940	17.12	119.6	0.629	6.99	4.2	5.99	2.34	2.35	−1.57	1.82	−1.08	9.43
16	338.99641	+33.98225	6.29	6908	6.90	56.1	0.045	5.85	4.4	5.05	1.86	2.10	−1.04	0.96	−2.09	9.94
17	338.99532	+33.98261	6.69	6924	7.56	80.4	0.096	6.18	3.6	4.98	1.87	2.73	−0.97	0.24	−1.82	9.69
18	338.99653	+33.98234	6.75	6935	6.65	70.0	0.050	5.89	4.6	4.77	1.71	2.16	−1.34	1.30	−2.11	9.82
19	338.99683	+33.98217	6.79	6919	8.41	87.7	0.126	6.29	3.7	5.08	1.92	2.62	−0.95	0.64	−2.26	10.18
20	338.99553	+33.98278	7.35	6940	8.93	102.3	0.218	6.53	2.8	5.17	2.02	2.47	−1.14	1.17	−1.33	9.35
21	338.99546	+33.98285	7.58	6943	5.17	66.1	0.041	5.80	3.2	4.54	1.67	1.96	−1.62	1.12	−0.91	8.58
22	338.99286	+33.98020	7.65	6033	4.63	98.9	0.074	6.06	2.1	4.18	1.58	2.01	−1.54	1.21	−1.25	8.83
23	338.99572	+33.98288	7.77	6934	12.16	45.1	0.027	5.63	18.3	5.60	1.83	2.73	−0.84	0.28	−1.80	9.63
24	338.99469	+33.98287	7.87	6947	6.22	86.1	0.101	6.20	2.5	4.75	1.83	2.33	−1.34	0.84	−1.87	9.70
25	338.99267	+33.98020	8.20	6011	10.87	56.3	0.071	6.05	7.0	5.63	2.05	2.49	−1.68	1.05	−1.41	9.46
26	338.99569	+33.98305	8.37	6894	13.08	62.4	0.087	6.13	9.1	5.75	2.05	2.68	−0.43	0.60	−1.78	9.83
27	338.99593	+33.98308	8.60	6927	7.10	77.9	0.119	6.27	2.5	5.06	1.99	2.22	−1.70	1.06	−1.99	9.98
28	338.99584	+33.98311	8.63	6930	3.77	58.1	0.027	5.62	2.3	4.25	1.60	0.95	−1.40	3.04	−1.96	9.55
29	338.99253	+33.98010	8.68	6008	6.31	47.6	0.030	5.67	4.7	5.01	1.82	2.40	−0.77	0.31	−1.27	9.09
30	338.99605	+33.98316	8.94	6868	3.09	69.0	0.023	5.55	2.2	3.78	1.38	1.81	−2.15	1.02	−2.02	9.40
31	338.99232	+33.98011	9.28	6011	2.69	73.4	0.026	5.60	1.5	3.63	1.37	1.89	−1.47	0.72	−0.98	8.35
32	338.99617	+33.98324	9.30	6871	6.35	48.1	0.023	5.55	6.4	4.88	1.69	2.55	−0.87	−0.12	−2.01	9.70
33	338.99590	+33.98333	9.45	6903	12.01	72.0	0.159	6.39	4.9	5.75	2.18	2.84	−0.93	0.30	−1.98	10.16
34	338.99596	+33.98334	9.51	6882	7.03	69.3	0.064	6.00	4.0	4.94	1.82	2.25	−1.92	1.04	−2.01	9.84
35	338.99166	+33.98205	11.91	6922	7.04	46.0	0.024	5.57	7.1	5.04	1.75	2.00	−1.20	1.30	−1.74	9.49
36	338.99092	+33.97975	13.64	6006	4.29	66.3	0.073	6.06	1.2	4.63	1.92	1.89	−1.11	1.24	−1.30	9.21

Notes.

[a] Distance from the center of the SQ-A starburst (R.A. = 338°.995333, decl. = +33°.98074).

[b] Redshift velocity.

[c] Velocity dispersion.

[d] Effective radius.

[e] Integrated CO(2–1) flux, with a ∼15% error dominated by the calibration uncertainty.

[f] Logarithm of M_{mol}, with an error of the order of a factor of ∼2 dominated by the uncertainty of the conversion factor α_{CO10}.

[g] Virial parameter.

[h] Logarithm of the external pressure divided by the Boltzmann constant.

[i] Logarithm of the molecular gas surface density.

[j] Logarithm of the S parameter (a measure of the projected specific angular momentum).

[k] Logarithm of the gradient of radial velocity.

[l] Logarithm of the C parameter (a measure of the ratio of nonrotational to rotational energy).

[m] Logarithm of the SFR surface density.

[n] Logarithm of the depletion timescale of the molecular gas ($t_{dep} = \Sigma_{mol}/\Sigma_{SFR}$).

$$\sigma_v = \sqrt{\sum_i f_i\,(v_i - v)^2}\,/\sum_i f_i. \tag{A4}$$

The effective radius of a clump is defined as

$$R_e = \sqrt{A_e/\pi} \tag{A5}$$

where A_e is the signal-weighted area of the clump in pc^2,

$$A_e = \frac{a_{\rm pix}\sum_i (f_i/f_{\rm peak})\,\delta v}{\sqrt{2\pi}\ \sigma_v} \tag{A6}$$

where $a_{\rm pix}$ is the pixel area in pc^2, $f_{\rm peak}$ the peak signal, and δv the velocity bin width. Here we assume that in the velocity dimension signals follow a Gaussian distribution characterized by $\sigma = \sigma_v$. $M_{\rm mol}$ is estimated from the integrated flux $f_{\rm CO21}$ assuming a CO conversion factor $\alpha_{\rm CO10} = 1.0\,M_\odot$ (K km s^{-1} pc^2)$^{-1}$. and a CO(2–1) to CO(1–0) luminosity ratio $r_{21} = L'_{\rm CO}(2-1)/L'_{\rm CO}(1-0) = 0.34$ (B. H. C. Emonts et al. 2025). The surface density $\Sigma_{\rm mol} = M_{\rm mol}/A_e$.

We define a 2D vector $\boldsymbol{S} = {\rm S}_x\boldsymbol{i} + {\rm S}_y\boldsymbol{j}$ to represent the contribution of the radial velocity to the projected specific angular momentum (i.e., the angular momentum per unit mass projected onto the plane perpendicular to the line of sight). Here S_x and S_y are the x- and y-components and $\boldsymbol{i}$ and $\boldsymbol{j}$ are unit vectors along the x- and y-axes, respectively (the cube is north-up, therefore the x-axis is directed west and the y-axis north). S, the absolute value of $\boldsymbol{S}$, is a scalar parameter in units of km s^{-1} pc:

$$S = \sqrt{S_x^2 + S_y^2} \tag{A7}$$

where

$$S_x = -d_{\rm pix}\frac{\sum_i f_i (v_i - v)(y_i - y)}{\sum_i f_i} \tag{A8}$$

$$S_y = d_{\rm pix}\frac{\sum_i f_i (v_i - v)(x_i - x)}{\sum_i f_i}, \tag{A9}$$

and $d_{\rm pix}$ is the pixel size in parsecs. We also define a C parameter as follows:

$$\mathrm{C} = (E - E_S)/E_{\rm S} \tag{A10}$$

where E is a measure of the specific kinematic energy per unit mass:

$$E = \frac{\sigma_v^2}{2} \tag{A11}$$

and E_s is a measure of the specific rotational energy:

$$E_S = \frac{S^2}{2J} \tag{A12}$$

where J is a measure of the specific rotational inertia:

$$J = \frac{d_{\rm pix}^2\sum_i f_i((x_i - x)^2 + (y_i - y)^2)}{\sum_i f_i}. \tag{A13}$$

By definition $E \geqslant E_S$, therefore $\mathrm{C} \geqslant 0$. Due to projection effects and beam smearing, E and E_S are not rigorous representations of the total kinematic and rotational energies, respectively. Nevertheless C can be used as an indicator of the ratio of nonrotational to rotational energy in a clump. When $C < 1$ the kinematics in the clump is likely dominated by rotation and when $C \gg 1$ it is dominated by nonrotational motions.

In order to study the effects of shear motion, we define a 2D vector $\boldsymbol{G}_v = G_{v,x}\boldsymbol{i} + G_{v,y}\boldsymbol{j}$ to represent the gradient of the radial velocity. Its absolute value, G_v, is a scalar parameter in units of km s^{-1} pc^{-1}:

$$G_v = \sqrt{G_{v,x}^2 + G_{v,y}^2} \tag{A14}$$

where

$$G_{v,x} = \frac{\sum_i w_i (v_i - v)/(x_i - x)}{d_{\rm pix}\sum_i w_i} \tag{A15}$$

$$G_{v,y} = \frac{\sum_i u_i (v_i - v)/(y_i - y)}{d_{\rm pix}\sum_i u_i}. \tag{A16}$$

In order to avoid runaway errors due to pixels with coordinates too close to those of the center of mass of the clump, we choose the following weights (i.e., w_i and u_i) in above summations:

$$\begin{aligned} w_i &= f_i \quad (\text{when } x_i - x > 0.5) \\ &= 0 \quad (\text{when } x_i - x \leqslant 0.5) \end{aligned} \tag{A17}$$

$$\begin{aligned} u_i &= f_i \quad (\text{when } y_i - y > 0.5) \\ &= 0 \quad (\text{when } y_i - y \leqslant 0.5). \end{aligned} \tag{A18}$$

The external pressure P_e is calculated as follows (B. G. Elmegreen 1989):

$$P_e = \frac{3\Gamma M_{\rm mol}\sigma_v^2}{4\pi R_e^3} \tag{A19}$$

where Γ is the ratio between the density at the edge of a clump and the average density. Following K. E. Johnson et al. (2015), we assume $\Gamma = 0.5$.

The virial parameter $\alpha_{\rm vir}$ is defined by

$$\alpha_{\rm vir} = \frac{5\sigma_v^2 R_e}{M_{\rm mol}G} \tag{A20}$$

where $G = 4.3 \times 10^{-3}$ is the gravitational constant in units of pc (km s^{-1})^2 $M_\odot^{-1}$.

The SFR surface density $\Sigma_{\rm SFR}$ is estimated using the JWST 15 μm data. Two operational issues make the estimation of $\Sigma_{\rm SFR}$ from integrated 15 μm flux over the actual sky area of a clump unfavorable: (1) many clumps are smaller than the 15 μm beam; (2) on the 2D image of the 15 μm emission many clumps are blended with each other. Therefore we adopt a simpler approach of measuring the peak 15 μm flux of each clump using a fixed aperture of $r = 0\farcs25$, which is approximately the resolution of the JWST 15 μm image (Section 2.3). The $f_{15\ \mu{\rm m}}$-to-SFR conversion is calibrated using the total 15 μm flux in the SQ-A region, which is 6.85 mJy, and the total SFR = 1.42 $M_\odot$ yr^{-1} (sum of SFRs of the three components listed in Table 1). This gives a $f_{15\ \mu{\rm m}}$-to-SFR conversion factor of 0.21 $M_\odot$ yr^{-1} mJy^{-1}. Then $\Sigma_{\rm SFR}$ is estimated using the ratio between the SFR value and the aperture area:

$$\Sigma_{\rm SFR} = \frac{\rm SFR}{A_{\rm aper}}, \tag{A21}$$

where $A_{\rm aper}$ is the area of the aperture ($r = 0\farcs25$) in kpc^2. Note that the SFR estimated from 15 μm flux may be contaminated

by shocked gas emission of the [N III] 15.56 μm line (Section 2.3). However, since that line is rather weak in shocked gas (with [N III]/[N II] ratio about an order of magnitude lower than that in SF regions; P. N. Appleton et al. 2025, in preparation), this contamination may be insignificant. Another uncertainty in using the 15 μm emission as an SFR indicator is due to possible destruction of small grains, which may result in an underestimate of the SFR. But, because we use the total SFR of SQ-A derived from extinction-corrected Hα data (S. Duarte Puertas et al. 2021) instead of the one measured from the 15 μm luminosity, the adopted $f_{15\mu m}$-to-SFR ratio should be unbiased on average. Nevertheless, there can still be substantial clump-to-clump variations of this ratio. Given the multiple uncertainties listed above, the error of the Σ_{SFR} so estimated is of the order of a factor of 2.

The depletion timescale t_{dep} is another SF activity indicator, defined as follows:

$$t_{dep} = \frac{\Sigma_{mol}}{\Sigma_{SFR}}. \quad \text{(A22)}$$

ORCID iDs

C. K. Xu https://orcid.org/0000-0002-1588-6700
C. Cheng https://orcid.org/0000-0003-0202-0534
M. S. Yun https://orcid.org/0000-0001-7095-7543
P. N. Appleton https://orcid.org/0000-0002-7607-8766
B. H. C. Emonts https://orcid.org/0000-0003-2983-815X
J. Braine https://orcid.org/0000-0003-1740-1284
S. C. Gallagher https://orcid.org/0000-0001-6217-8101
P. Guillard https://orcid.org/0000-0002-2421-1350
U. Lisenfeld https://orcid.org/0000-0002-9471-5423
E. O'Sullivan https://orcid.org/0000-0002-5671-6900
F. Renaud https://orcid.org/0000-0001-5073-2267
P. Aromal https://orcid.org/0009-0001-2178-4022
P.-A. Duc https://orcid.org/0000-0003-3343-6284
A. Labiano https://orcid.org/0000-0002-0690-8824
A. Togi https://orcid.org/0000-0001-5042-3421

References

Abe, D., Inoue, T., Inutsuka, S., & Matsumoto, T. 2021, ApJ, 916, 83
Adamo, A., Hollyhead, K., Messa, M., et al. 2020, MNRAS, 499, 3267
Alatalo, K., Appleton, P. N., Lisenfeld, U., et al. 2014, ApJ, 795, 159
Allen, R. J., & Hartsuiker, J. W. 1972, Natur, 239, 324
Appleton, P. N., Guillard, P., Boulanger, F., et al. 2013, ApJ, 777, 66
Appleton, P. N., Guillard, P., Emonts, B., et al. 2023, ApJ, 951, 104
Appleton, P. N., Xu, C. K., Reach, W., et al. 2006, ApJL, 639, L51
Arnaudova, M. I., Das, S., Smith, D. J. B., et al. 2024, MNRAS, 535, 2269
Arp, H. 1995, ApJ, 183, 411
Berry, D. 2015, A&C, 10, 22
Berry, D. S., Reinhold, K., Jenness, T., & Economou, F. 2007, in ASP Conf. Ser. 376, Astronomical Data Analysis Software and Systems XVI, ed. R. A. Shaw, F. Hill, & D. J. Bell (San Francisco, CA: ASP), 425
Bolatto, A. D., Wolfire, M., & Leroy, A. K. 2013, ARA&A, 51, 207
Braine, J., Davoust, E., Zhu, M., et al. 2003, A&A, 408, L13
Braine, J., Hughes, A., Rosolowsky, E., et al. 2020, A&A, 663, A17
Braine, J., Rosolowsky, E., Gratier, P., et al. 2018, A&A, 612, A51
Briggs, D. S. 1995, PhD thesis, New Mexico Institute of Mining and Technology
Cao, C., Xu, C. K., Domingue, D., et al. 2016, ApJS, 222, 16
CASA Team, Bean, B., Bhatnagar, S., et al. 2022, PASP, 134, 114501
Cheng, C., Xu, C. K., Appleton, P. N., et al. 2023, ApJ, 954, 74
Cluver, M. E., Appleton, P. N., Boulanger, F., et al. 2010, ApJ, 710, 248
Currie, M. J., Berry, D. S., Jenness, T., et al. 2014, in ASP Conf. Ser. 485, Astronomical Data Analysis Software and Systems XXIII, ed. N. Manset & P. Forshay (San Francisco, CA: ASP), 391
Dicken, D., Marín, M. G., Shivaei, I., et al. 2024, A&A, 689, A5
Donovan Meyer, D., Koda, J., Momose, R., et al. 2013, ApJ, 772, 107
Downes, D., & Solomon, P. M. 1998, ApJ, 507, 615
Duarte Puertas, S., Iglesias-Paramo, J., Vilchez, J. M., et al. 2019, A&A, 629, 102
Duarte Puertas, S., Vilchez, J. M., Iglesias-Paramo, J., et al. 2021, A&A, 645, 57
Duc, P.-A., Cuillandre, J.-C., & Renaud, F. 2018, MNRAS, 475, L40
Elmegreen, B. G. 1989, ApJ, 338, 178
Elmegreen, B. G. 1998, in ASP Conf. Ser. 148, Origins, ed. C. E. Woodward, J. M. Shull, & H. A. Thronson, Jr (San Francisco, CA: ASP), 150
Emonts, B. H. C., Appleton, P. N., Lisenfeld, U., et al. 2025, ApJ, 978, 111
Federrath, C., & Klessen, R. S. 2012, ApJ, 761, 156
Fedotov, K., Gallagher, S. C., Konstantopoulos, I. S., et al. 2011, AJ, 142, 42
Fukui, Y., Habe, A., Inoue, T., et al. 2021, PASJ, 73, S1
Fukui, Y., Torii, K., Hattori, Y., et al. 2018, ApJ, 859, 166
Fukui, Y., Tsuge, K., Sano, H., et al. 2017, PASJ, 69, 5
Gallagher, S. C., Charlton, J. C., Hunsberger, S. D., et al. 2001, AJ, 122, 163
Gao, Y., & Xu, C. 2000, ApJL, 542, L83
Guillard, P., Appleton, P. N., Boulanger, F., et al. 2022, ApJ, 925, 63
Guillard, P., Boulanger, F., Pineau des Forets, G., et al. 2009, A&A, 502, 515
Guillard, P., Boulanger, F., Pineau des Forêts, G., et al. 2012, ApJ, 749, 158
Habe, A., & Ohta, K. 1992, PASJ, 44, 203
Heyer, M., Krawczyk, C., Duval, J., & Jackson, J. M. 2009, ApJ, 699, 1092
Hibbard, J. E., van der Hulst, J. M., Barnes, J. E., & Rich, R. M. 2001, AJ, 122, 2969
Hickson, P. 1982, ApJ, 255, 382
Hunter, T. R., Indebetouw, R., Brogan, C. L., et al. 2023, PASP, 135, 074501
Hwang, J.-S., Struck, C., Renaud, F., & Appleton, P. N. 2012, MNRAS, 419, 1780
Iglesias-Páramo, J., López-Martín, L., Vílchez, J. M., Petropoulou, V., & Sulentic, J. W. 2012, A&A, 539, A127
Iglesias-Paramo, J., & Vilchez, J. M. 2001, ApJ, 550, 204
Inoue, T., & Fukui, Y. 2013, ApJL, 774, 31
Iono, D., Yun, M. S., & Ho, P. T. P. 2005, ApJS, 158, 1
Johnson, K. E., Hibbard, J. E., Gallagher, S. C., et al. 2007, AJ, 134, 1522
Johnson, K. E., Leroy, A. K., Indebetouw, R., et al. 2015, ApJ, 806, 35
Kennicutt, R. C. 1998, ARA&A, 36, 189
Kessler, M. F., Steinz, J. A., Anderegg, M. E., et al. 1996, A&A, 315, L27
Kim, J., Chevance, M., Kruijssen, J. M. D., et al. 2022, MNRAS, 516, 3006
Klein, R., McKee, C. F., & Colella, P. 1994, ApJ, 420, 213
Krahm, G., Finn, M. K., Indebetouw, R., et al. 2024, ApJ, 964, 166
Kruijssen, J. M. D., Schruba, A., Hygate, A. P. S., et al. 2018, MNRAS, 479, 1866
Krumholz, M. R. 2014, PhR, 539, 49
Leroy, A. K., Sun, J., Meidt, S., et al. 2025, ApJ, 985, 14
Li, C., Wang, H. C., Wu, Y. W., et al. 2020, RAA, 20, 031
Libralato, M., Argyriou, I., Dicken, D., et al. 2024, PASP, 136, 034502
Lisenfeld, U., Braine, J., Duc, P.-A., et al. 2002, A&A, 394, 823
Lisenfeld, U., Xu, C. K., Gao, Y., et al. 2019, A&A, 627, A107
Maeda, R., Inoue, T., & Fukui, Y. 2021, ApJ, 908, 2
Maeda, R., Inoue, T., Omukai, K., et al. 2024, ApJ, 971, 62
McKee, C. F., & Kowie, L. L. 1975, ApJ, 195, 715
Mendes de Oliveira, C., Plana, H., Amram, P., et al. 2001, AJ, 121, 2524
Moles, M., Marquez, I., & Sulentic, J. W. 1998, A&A, 334, 473
Moles, M., Sulentic, J. W., & Marquez, I. 1997, ApJL, 485, 69
Orkisz, J. H., Jerome, P., Gerin, M., et al. 2017, A&A, 599, 99
O'Sullivan, E., Giacintucci, S., Vrtilek, J. M., et al. 2009, ApJ, 701, 1560
Petkova, M. A., Kruijssen, J. M. D., Henshaw, J. D., et al. 2023, MNRAS, 525, 962
Pontoppidan, K. M., Barrientes, J., Blome, C., et al. 2022, ApJL, 936, L14
Rani, R., Moore, T. J. T., Eden, D. J., & Rigby, A. J. 2022, MNRAS, 515, 271
Renaud, F., Appleton, P. N., & Xu, C. K. 2010, ApJ, 742, 80
Renaud, F., Bournaud, F., Daddi, E., et al. 2019, A&A, 621, A104
Renaud, F., Bournaud, F., Kraljic, K., & Duc, P. A. 2014, MNRAS, 442, L33
Rodríguez-Baras, M., Rosales-Ortega, F. F., Díaz, A. I., Sánchez, S. F., & Pasquali, A. 2014, MNRAS, 442, 495
Sanders, D. B., & Mirabel, I. F. 1996, ARA&A, 34, 749
Shostak, G. S., Sullivan, W. T., & Allen, R. J. 1984, A&A, 139, 15
Solomon, P. M., Rivolo, A. R., Barrett, J., & Yahil, A. 1987, ApJ, 319, 730
Sulentic, J. W., Rosado, M., Dultzin-Hacyan, D., et al. 2001, AJ, 122, 2993
Takahira, K., Tasker, E. J., & Habe, A. 2014, ApJ, 792, 63
Trinchieri, G., Sulentic, J., Breitschwerdt, D., et al. 2003, A&A, 401, 173
Tsuge, K., Fukui, Y., Tachihara, K., et al. 2021a, PASJ, 73, S35

Tsuge, K., Sano, H., Tachihara, K., et al. 2024, PASJ, 76, 589
Tsuge, K., Tachihara, K., Fukui, Y., et al. 2021b, PASJ, 73, 417
Valentino, F., Brammer, G., Gould, K. M. L., et al. 2023, ApJ, 947, 20
Verdes-Montenegro, L., Yun, M. S., Williams, B. A., et al. 2001, A&A, 377, 812
Whitmore, B. C., & Schweizer, F. 1995, AJ, 109, 960
Williams, B. A., Yun, M. S., & Verdes-Montenegro, L. 2002, AJ, 123, 2471
Wilson, C. D., Scoville, N., Madden, S. C., & Charmandaris, V. 2000, ApJ, 542, 120
Xu, C., Gao, Y., Mazzarella, J., et al. 2000, ApJ, 541, 644
Xu, C., Sulentic, J. W., & Tuffs, R. 1999, ApJ, 512, 178
Xu, C. K., Cheng, C., Appleton, P. N., et al. 2022, Natur, 610, 461
Xu, C. K., Domingue, D., Cheng, Y., et al. 2010, ApJ, 713, 330
Xu, C. K., Iglesias-Paramo, J., Burgarella, D., et al. 2005, ApJL, 619, L95
Xu, C. K., Lisenfeld, U., Gao, Y., & Renaud, F. 2021, ApJ, 918, 55
Xu, C. K., Lu, N., Condon, J. J., et al. 2003, ApJ, 595, 665
Yun, M. S., Verdes-Montenegro, L., del Olmo, A., & Perea, J. 1997, ApJL, 475, 21
Zhu, M., Gao, Y., Seaquist, E. R., et al. 2007, AJ, 134, 118